Hot-wire spatial resolution issues in wall-bounded turbulence

N. HUTCHINS[1]†, T. B. NICKELS[2], I. MARUSIC[1] AND M. S. CHONG[1]

[1]Walter Bassett Aerodynamics Laboratory, Department of Mechanical Engineering, University of Melbourne, Victoria 3010, Australia

[2]Department of Engineering, University of Cambridge, Trumpington Street, Cambridge CB2 1PZ, UK

Careful reassessment of new and pre-existing data shows that recorded scatter in the hot-wire-measured near-wall peak in viscous-scaled streamwise turbulence intensity is due in large part to the simultaneous competing effects of the Reynolds number and viscous-scaled wire length l^+. An empirical expression is given to account for these effects. These competing factors can explain much of the disparity in existing literature, in particular explaining how previous studies have incorrectly concluded that the inner-scaled near-wall peak is independent of the Reynolds number. We also investigate the appearance of the so-called outer peak in the broadband streamwise intensity, found by some researchers to occur within the log region of high-Reynolds-number boundary layers. We show that the 'outer peak' is consistent with the attenuation of small scales due to large l^+. For turbulent boundary layers, in the absence of spatial resolution problems, there is no outer peak up to the Reynolds numbers investigated here ($Re_\tau = 18\,830$). Beyond these Reynolds numbers – and for internal geometries – the existence of such peaks remains open to debate. Fully mapped energy spectra, obtained with a range of l^+, are used to demonstrate this phenomenon. We also establish the basis for a 'maximum flow frequency', a minimum time scale that the full experimental system must be capable of resolving, in order to ensure that the energetic scales are not attenuated. It is shown that where this criterion is not met (in this instance due to insufficient anemometer/probe response), an outer peak can be reproduced in the streamwise intensity even in the absence of spatial resolution problems. It is also shown that attenuation due to wire length can erode the region of the streamwise energy spectra in which we would normally expect to see k_x^{-1} scaling. In doing so, we are able to rationalize much of the disparity in pre-existing literature over the k_x^{-1} region of self-similarity. Not surprisingly, the attenuated spectra also indicate that Kolmogorov-scaled spectra are subject to substantial errors due to wire spatial resolution issues. These errors persist to wavelengths far beyond those which we might otherwise assume from simple isotropic assumptions of small-scale motions. The effects of hot-wire length-to-diameter ratio (l/d) are also briefly investigated. For the moderate wire Reynolds numbers investigated here, reducing l/d from 200 to 100 has a detrimental effect on measured turbulent fluctuations at a wide range of energetic scales, affecting both the broadband intensity and the energy spectra.

† Email address for correspondence: nhu@unimelb.edu.au

1. Introduction

The spatial attenuation owing to an idealized spanwise sensor (which measures streamwise velocity u) is, in principle, a simple function of the evaluated integral of velocity fluctuation across that transverse element. For turbulent flows, this process is complicated by the fact that the velocity fluctuations are time dependent and are composed instantaneously of multiple overlapping and interacting scales. In wall-bounded turbulence these velocity fluctuations are also highly anisotropic and subject to complex, and often disputed, scaling conditions, both of which raise questions over the applicability of isotropic assumptions in providing theoretical corrections (e.g. Wyngaard 1968). As such, the degree of attenuation due to the single spanwise element will be highly dependent on the spectral composition of the turbulent fluctuations. Specifically, we must consider the width of the energetic fluctuations, as compared to the spanwise integral length of the sensor element. Since isotropic assumptions are not really applicable in boundary layers (other than for very high wavenumbers), this requires spectral information in the spanwise direction (i.e. we need the energy contribution at each spanwise wavenumber k_y). In general, such information is not readily available from experiment (although it could, in theory, be obtained from detailed spanwise correlation measurements). In the interim, we can look to direct numerical simulations (DNS), which indicate that the spanwise spectral composition of u fluctuation is a complex function of distance from the wall (z) and the Reynolds number Re (see for instance Abe, Kawamura & Choi 2004; del Álamo *et al.* 2004; Kasagi, Fukagata & Suzuki 2005; Hutchins & Marusic 2007a). Until such time that realistic functional forms exist to describe this energy content for a given z and Reynolds number, the onus will continue to rest with experimental data in providing guidelines for spatial attenuation of hot-wire sensors. Throughout this paper, x, y and z will be used to denote the streamwise, spanwise and wall-normal axes, with u, v and w denoting the respective fluctuating velocity components.

Of the numerous experimental investigations of spatial resolution, that of Ligrani & Bradshaw (1987, hereinafter referred to as LB87) is by far the most cited. Their introduction also provides an excellent review of the literature on this subject. Through exhaustive parametric study of wire length (l) and the length-to-diameter ratio (l/d) they argue two compelling recommendations for accurate hot-wire measurements in turbulent boundary layers; namely that the viscous-scaled wire length (l^+) should be less than 20 and that the length-to-diameter ratio should be greater than 200. As a cautionary note, the experiments of LB87 were conducted at a single, quite low, Reynolds number and investigated just the attenuation in the immediate near-wall region of the boundary layer. Since we would expect the actual attenuation to be a function of the spectral composition of the velocity fluctuations (a complex function of z and Re), it becomes questionable how applicable the recommendations of LB87 will be to higher Reynolds numbers and away from the near wall.

Several other researchers have experimentally investigated the effects of sensor length on the measured near-wall velocity fluctuations (e.g. Johansson & Alfredsson 1983; Willmarth & Sharma 1984; Hites 1997; Österlund 1999), although with the exception of Hites, few have repeated the LB87 approach of several different wire lengths at a single constant Reynolds number. Hence the information on this subject is somewhat fragmented across multiple studies, each of which provides limited (often conflicting) insight into the larger picture. Following the insightful approach of Klewicki & Falco (1990), we here attempt to redress this problem. In §3, we consider simultaneously the effects of the Reynolds number and wire length at a single (viscous-scaled) distance from the wall (close to the peak in the broadband

turbulence intensity) and compile the available data from the various studies into a single reference.

The two decades since the publication of LB87 have seen an increase in the availability of higher-Reynolds-number turbulent wall-bounded flow data, for example from the Princeton superpipe (Morrison *et al.* 2004), the National Diagnostic Facility at Illinois Institute of Technology in Chicago (Hites 1997), the minimum turbulence level (MTL) wind tunnel at KTH in Stockholm (Österlund 1999), the High Reynolds Number Boundary Layer Wind Tunnel (HRNBLWT) at the University of Melbourne (Nickels *et al.* 2007) and the large low-speed facility (LLF) at DNW in the Netherlands (Fernholz *et al.* 1995). One of the widely discussed facets of these results has been the emergence of a secondary outer peak in the log region of some of the higher-Reynolds-number broadband turbulent intensity profiles (Fernholz *et al.* 1995; Morrison *et al.* 2004). However, it is noted that these studies have tended to involve substantial relaxation of the key recommendations of LB87 for hot-wire design. Thus, the need to extend the spatial resolution findings of LB87 to higher Reynolds numbers (as attempted here) is particularly pertinent, as is the need to investigate the effects of spatial resolution away from the immediate near-wall region, on which matter very little has to date been published. In light of this, we have here (in §§ 4 and 5) set out to address in detail the wider effects of spatial resolution on fluctuating statistics and energy spectra throughout the log region of turbulent boundary layers.

Though not strictly a spatial resolution corollary, the issue of wire length-to-diameter ratio is to some extent bound with the requirement for ever-smaller sensor lengths as the Reynolds number is increased. At high *Re*, it is obviously tempting to maintain small l^+ by relaxing l/d rather than using smaller wire diameters (with attendant loss of mechanical strength). One problem with this approach is that additional heat is lost to the sensor supports, and this leads to an attenuation of measured stresses. The proportion of heat lost to the supports depends on both l/d and the Reynolds number of the sensor. From their experiments, LB87 suggested a limit of $l/d > 200$, but this was for a single Reynolds number. Recent numerical studies by Li *et al.* (2004) have shown that the proportion of heat loss to the supports can be maintained at acceptable levels for lower l/d values if the wire Reynolds number is increased, but the precise limits for real hot-wire measurements are still not clear. In § 7 we attempt to redress this shortfall, using sensors with deliberately inadequate l/d to explore the wider effects of the length-to-diameter ratio on the log-region turbulence intensity and energy spectra.

Occasionally it is difficult to separate the effects due to spatial resolution from those due to a temporal attenuation of the fluctuating signals. In § 8 we introduce the notion of a maximum flow frequency. This frequency describes the minimum energetic time scale that we are likely to encounter in near-wall turbulent boundary layers. (Certain dissipative scales might have even smaller time scales but, these are not expected to contribute significantly to the measured broadband intensity.) In § 8 we investigate the consequences for the measured streamwise energy, when these time scales are not fully resolved.

Throughout this study, we have limited ourselves to consideration of single spanwise-normal hot wires in a turbulent boundary layer. However, in a more limited sense, many of the findings ought to be in some way applicable to more complex probe geometries and wire orientations, as well as providing insight on spatial attenuation owing to finite interrogation volumes/areas in particle image velocimetry (PIV), laser Doppler velocimetry (LDV) and pressure-based velocimetry experiments.

2. Apparatus

2.1. *Facility*

Experiments were conducted in the HRNBLWT. This is an open-return blower wind tunnel with a working section of $27 \times 2 \times 1$ m. Measurements are made on the tunnel floor, between 5 and 21 m downstream of the tripped inlet. The tunnel floor is constructed from 6 m sections of polished aluminium plate with a root-mean-square surface roughness that is not greater that 0.1 viscous length scales (ν/U_τ, where ν is kinematic viscosity and U_τ is the friction velocity). The pressure gradient is nominally zero, with pressure coefficient (C_p) variation along the entire 27 m length set to within $\pm 1.0\,\%$ at 10 m s^{-1} ($Re_\tau \approx 7300$) and $\pm 0.7\,\%$ at 20 and 30 m s^{-1} ($Re_\tau \approx 14\,000$ and $19\,000$ respectively). Further details of the facility are available in Nickels *et al.* (2005, 2007).

2.2. *Constant-temperature anemometry*

With the exception of the measurement at $Re_\tau = 18\,830$, the hot-wire probes are all operated in constant-temperature mode using the AN-1003 anemometer (AA Lab Systems) with overheat ratio 1.8. All channels are option 01, 04 and 12 equipped (i.e. they have ultra-low noise amplifier, are frequency compensated and have high-performance signal conditioner). The indicated frequency response of the system to a 2 kHz internal pulse varied from 70 to 100 kHz (for a description of electronic testing of anemometer response, see Freymuth 1977*a*). For the smallest diameter wires ($d = 1.5\,\mu$m) which were required at $Re_\tau = 18\,830$, it was not possible to balance the AN-1003. In this instance we reverted to the in-house Melbourne University Constant Temperature Anemometer (MUCTA II) which in this set-up gave an indicated system frequency response to a 1 kHz external square wave of 135 kHz. Hot-wire signals were sampled using a Microstar DAP3000a/21 14-bit data-acquisition board. Sampling frequencies and low-pass filter settings are given in table 1 along with sample intervals. The hot wires are statically calibrated *in situ* against a Pitot-static tube pair before and after each boundary-layer traverse. Third-order polynomial curves are fitted to the calibration data. Atmospheric conditions are monitored continuously throughout the experiments using a calibrated thermocouple and an electronic barometer (144S-BARO, Sensortechnics). Linear interpolation between the pre- and post-calibration curves is used to correct for temperature drift during the course of the experiment. Free-stream velocity U_∞ is also monitored throughout the course of the experiment using the same Pitot-static tube pair. If the final hot-wire velocity reading in the free stream (from the temperature-compensated calibration curve) does not match the Pitot-static-measured U_∞ to within $\pm 0.5\,\%$, the entire dataset is discarded (which very rarely happens with the 2.5 and 5 μm wires).

2.3. *Probes*

Platinum sensing elements are fabricated to two boundary-layer-type probe-body geometries: Dantec 55P05 or 55P15 with prong spacings of 3 and 1.25 mm respectively. Wollaston wires (of various core diameters d) are soldered to the prong tips and etched to give a platinum filament of the desired length (l). For the very long wire lengths, a 55P05 probe body has been modified to give an overall prong spacing of 5 mm.

2.4. *Experimental conditions*

Table 1 gives the full range of experimental conditions and probe/sensor geometries; U_∞ is the free-stream velocity and U_τ is the friction velocity, determined from a Clauser fit to the logarithmic portion of the mean velocity data (using constants $\kappa = 0.41$ and

U_∞ (ms^{-1})	x (m)	Re_τ	ν/U_τ (μm)	δ (m)	probe	l (mm)	l^+	d (μm)	l/d	t^+	f_s (kHz)	f_{lp} (kHz)	TU_∞/δ	$|l/\eta|_{z=0.1\delta}$
11.97	5	2820	35.0	0.098	55P05	0.76	22†	3.8	200	0.53	24.07	12	14 600	6.7
11.87	8	3910	36.0	0.140	55P05	0.76	21†	3.8	200	0.49	24.07	12	15 200	5.9
10.30	21	7340	44.0	0.319	55P05	1.00	23†	5.0	200	0.34	24.07	12	17 400	5.0
20.54	21	13 620	23.0	0.315	55P15	0.50	22†	2.5	200‡	0.48	60.06	30	15 700	4.5
30.20	21	18 830	16.0	0.303	55P15	0.35	22†	1.5	233	0.59	101.01	50	12 000	4.2
11.96	5	2 870	35.0	0.099	55P05	1.00	29	5	200	0.53	24.07	12	14 400	8.8
17.24	5	3840	25.0	0.096	55P05	0.76	30	3.8	200	0.41	60.06	30	16 100	8.5
17.25	5	3860	25.0	0.097	55P05	1.00	40	5	200	0.41	60.06	30	16 000	11.3
10.29	21	7370	43.7	0.322	55P15	0.50	11	2.5	200	0.33	24.07	12	17 200	2.6
10.06	21	7440	44.1	0.328	special	3.50	79	5.0	700	0.37	20.83	10	20 200	18.9
13.00	21	9160	35.4	0.324	55P01	1.80	51	5.0	360	0.58	20.83	10	12 000	11.6
13.56	21	9750	33.6	0.327	55P01	1.25	37	5.0	250	0.64	20.83	10	27 300	8.3
20.02	21	13 880	23.4	0.325	55P15	0.50	22	5.0	100‡	0.67	40.67	20	14 800	4.5
20.04	21	13 220	23.4	0.310	55P15	0.50	22	12.7	39‡	0.69	40.16	20	7 800	4.6
20.52	21	13 530	23.1	0.313	55P05	1.00	43	5.0	200	0.48	60.06	30	15 700	8.9
20.04	21	14 020	22.7	0.318	55P05	1.80	79	5.0	360	0.69	40.67	20	15 300	16.1
20.04	21	13 900	22.8	0.317	special	3.50	153	5.0	700	0.69	40.67	20	15 200	31.3
30.05	21	20 270	15.6	0.316	55P05	1.80	116	5.0	360	1.49	40.67	20	14 300	21.6

TABLE 1. Experimental parameters for hot-wire experiments.

† Matched l^+ data.
‡ Matched l^+ and Re_τ data for l/d investigation.

Hot-wire anemometry spatial resolution

$A = 5.0$). Hot-wire-measured mean velocities can only be considered accurate to (at best) 1 % (see for example Jørgensen 1996). This error will be included in the U_τ estimate from the Clauser method, along with additional errors due to the regression fit. In addition, the precise choice of constants for the logarithmic region are also under debate (Nagib & Chauhan 2008). Use of the Clauser technique with altered constants (κ and A) will yield different estimates of U_τ. For the highest Reynolds-number data measured here, the use of $\kappa = 0.384$ and $A = 4.173$ as suggested by Nagib & Chauhan (2008) yields a value of U_τ that is 1.2 % lower than that obtained with $\kappa = 0.41$ and $A = 5.0$. (The difference is less severe at lower Reynolds numbers.) Capitalized velocities (e.g. U) and overbars indicate time-averaged values. The superscript $+$ is used to denote viscous scaling of length (e.g. $z^+ = z U_\tau / \nu$), velocities ($U^+ = U/U_\tau$) and time ($t^+ = t U_\tau^2 / \nu$). The friction Reynolds number Re_τ (also known as the Kármán number) is given by $\delta U_\tau / \nu$, where δ is the boundary-layer thickness determined from a modified Coles law of the wall/wake fit to the mean velocity profile (see Perry, Marusic & Jones 2002). It must be noted that all boundary-layer traverses described here have logarithmic wall-normal spacing, and thus the spacing towards the edge of the boundary layer is quite large. For this reason the estimate of δ should only be considered accurate to ± 4 %. This uncertainty will extend to Re_τ. The length of the platinum sensing element is given by l and l^+ ($= l U_\tau / \nu$) in physical and viscous-scaled units respectively. The wire diameter is given by d and the length-to-diameter ratio by l/d. The sampling frequency and low-pass filter settings are denoted by f_s and f_{lp} respectively. The non-dimensional sample interval is given by $\Delta t^+ (= \Delta t U_\tau^2 / \nu$, where $\Delta t = 1/f_s$). The total length in seconds of the velocity sample at each height is given by T. This is non-dimensionalized in outer scaling to give boundary-layer turnover times $T U_\infty / \delta$. For converged statistics, these numbers need to be large. The largest structures in boundary layers can commonly exceed 20δ (Kim & Adrian 1999; Hutchins, Ganapathisubramani & Marusic 2004; Ganapathisubramani, Clemens & Dolling 2006; Guala, Hommema & Adrian 2006; Hutchins & Marusic 2007b; Monty *et al.* 2007), and we would typically require several hundreds of these events to advect past the sensor array before we could expect converged statistics. For facilities such as the HRNBLWT, where high Reynolds numbers are attained with a very thick boundary layer and relatively low flow speeds (ensuring a large viscous scale), this requires sampling for up to 10 minutes at each wall-normal station (total experiment times of up to 11 hours per traverse). For completeness, table 1 also includes the ratio of the sensor length to an estimate of the Kolmogorov length scale (η). Estimates for η are problematic, especially in boundary layers in which η varies with wall-normal position. Here, following Morrison *et al.* (2004), we use an estimate of η at $z/\delta = 0.1$ using the local-equilibrium approximation of the dissipation rate.

3. The near-wall peak in streamwise turbulence intensity

One issue of some controversy in wall-bounded turbulence has been that of the near-wall peak in inner-scaled streamwise broadband turbulent energy ($\overline{u^2}/U_\tau^2 |_m$). The subscript m refers to the peak value. Whilst there appears to be good general agreement concerning the inner-scaled wall-normal location of this peak (with $z_m^+ \approx 15 \pm 1$ widely reported), the measured magnitude continues to exhibit significant variation between studies. There are numerous factors that could contribute to this error, and a detailed discussion of these is given in §3.3. For now we concentrate on the two most significant of these: non-dimensional wire length (l^+) and the Reynolds
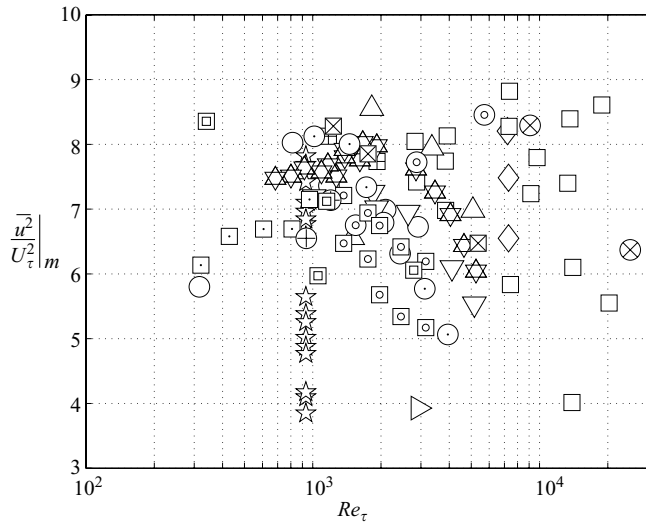
Purtell *et al.* (1981)		Nickels *et al.* (2007)	○		◇
Current study		Ligrani & Bradshaw (1987)	□		☆
Morrison *et al.* (2004)†		Hutchins & Marusic (2007*a*)	△		▽
Österlund (1999)‡	✴	Balint *et al.* (1991)¶			⊕
Monty (2005)	⊙	Erm & Joubert (1991)			⊡
Fernholz *et al.* (1995)	⊗	Andreopoulos *et al.* (1984)			⊠
Löfdahl *et al.* (1989)	▷	Bhatia *et al.* (1982)			⊞
Hites (1997)‖	◉	Hites (1997)††			⊡
Johansson & Alfredsson (1983)‡‡	⊡				

† Only $l/d = 200$ data; ‡only $d = 1.25$ μm and $d = 2.50$ μm data;
¶ nine-sensor vorticity probe; ‖ tunnel floor, data only available
at $z^+ \approx 24$ for highest two Re_τ; †† Smooth cylinder, have not
included $d = 1.3$ μm; ‡‡ Hot-film measurments in water, $l/d \approx 20$.

FIGURE 1. Reynolds-number variation of the peak measured value of the inner-scaled
streamwise turbulence intensity ($\overline{u^2}/U_\tau^2|_m$) for various hot-wire experiments.

number (Re). In a study that has become the benchmark for hot-wire design, LB87 have definitively shown that l^+ can significantly effect the measured values of $\overline{u^2}/U_\tau^2|_m$. Their results were obtained at a single Reynolds number. More recently there has been a growing acceptance that the near-wall peak does not scale exclusively with U_τ and instead exhibits a weak Re dependence (Klewicki & Falco 1990; DeGraaff & Eaton 2000; Metzger & Klewicki 2001; Metzger *et al.* 2001; Marusic & Kunkel 2003). A large outer-scale influence on the near-wall region becomes increasingly noticeable with Reynolds number, as a result of which $\overline{u^2}/U_\tau^2|_m$ has been found to increase with Re (see for example Hutchins & Marusic 2007*a*). In order to discern this trend the above studies attempted to isolate wire-length effects by considering only the data acquired with $l^+ \lesssim 10$ (with the exception of Klewicki & Falco 1990, who applied a correction for l^+).

3.1. *The near-wall peak as a function of l^+ and the Reynolds number*

For figure 1 we compile data for $\overline{u^2}/U_\tau^2|_m$ from numerous studies over a wide range of l^+ and plot these against Re_τ. The inclusion of higher-l^+ data tends to afford

us access to higher-Reynolds-number results. The provisos for inclusion were quite broad. We sought out quality measurements (attention to pressure gradient, free-stream turbulence and the like) made with single normal hot-wire sensors in which $l/d > 200$ (in order to isolate the effects of l/d; see LB87 and §7). Certain data are discarded. The data of Ueda & Hinze (1975), often cited, are not included due to insufficient l/d. The higher-Reynolds-number superpipe data of Morrison *et al.* (2004) and the very short wires of Willmarth & Sharma (1984) are discounted for similar reasons. We do not include those data of Österlund (1999) which are tabulated as having $d = 1.27 \, \mu\text{m}$. The $d = 1.3 \, \mu\text{m}$ data of Hites (1997) are not included, in deference to the calibration drift reported. It should be noted that figure 1 includes data from both external and internal flows (the latter of which will have non-zero streamwise pressure gradients). Further discussion of these effects is given in §3.3.2.

Plotted against Re_τ, the scatter in $\overline{u^2}/U_\tau^2|_m$ shown in figure 1 is large. There is some indication that the peak intensity might be rising with the Reynolds number, but for the most part this is obscured within the large scatter of data. The key to understanding this plot is to consider simultaneously the effects of l^+ and the Reynolds number on the near-wall peak in streamwise intensity. When figure 1 is replotted in three dimensions with l^+ as the z ordinate, as shown in figure 2(*a*), the data appear to collapse down rather well on to a surface. For clarity, figure 2(*b*) shows an amended version of the original plot, with each symbol coloured according to l^+ (with the colour-scale given to the right of the plot). The colour contours displayed in the background (and the mesh surface in figure 2*b*) show the best fit to the compiled data obtained by nonlinear least squares regression fit to the form

$$\left. \frac{\overline{u^2}}{U_\tau^2} \right|_m = A \log_{10} Re_\tau - B l^+ - C \left(\frac{l^+}{Re_\tau} \right) + D \tag{3.1}$$

A	1.0747	B	0.0352
C	23.0833	D	4.8371

Term 1 of this equation assumes that in the absence of spatial resolution effects, the near-wall peak in streamwise intensity will grow log linearly in Re_τ (in accordance with Metzger *et al.* 2001; Marusic & Kunkel 2003). Term 2 assumes a linear decay in the near-wall peak due to increasing l^+. A linear decay was chosen based on an initial analysis of the experimental data at higher Reynolds numbers (see figure 4). Term 3 is an l/δ term and accounts for attenuation of δ-scaled events by wires in which l is a substantial portion of the boundary-layer thickness. This term provides the requisite twist to the surface at low Reynolds number.

The compiled data cover the range $3 < l^+ < 153$ and $316 < Re_\tau < 25\,000$ (although the coverage of data is by no means homogeneous within this range). The root-mean-square residual error for this surface fit is 0.6 in predicted $\overline{u^2}/U_\tau^2|_m$. Of course, this surface fit is an oversimplification, and there are obvious outliers. See §3.3 for a more thorough discussion of the limitations of this fit. For now however, as a first attempt at fitting to limited scattered data, the surface given by (3.1) can explain some interesting trends in past results.

The solid black symbols in figure 2(*b*) show DNS channel-flow data of Iwamoto *et al.* (2002), del Álamo *et al.* (2004) and Moser, Kim & Mansour (1999). As a simple first-order approximation we might equate the spanwise grid spacing Δy in simulations to wire length l. For all DNS data shown in figure 2(*b*), the grid spacing
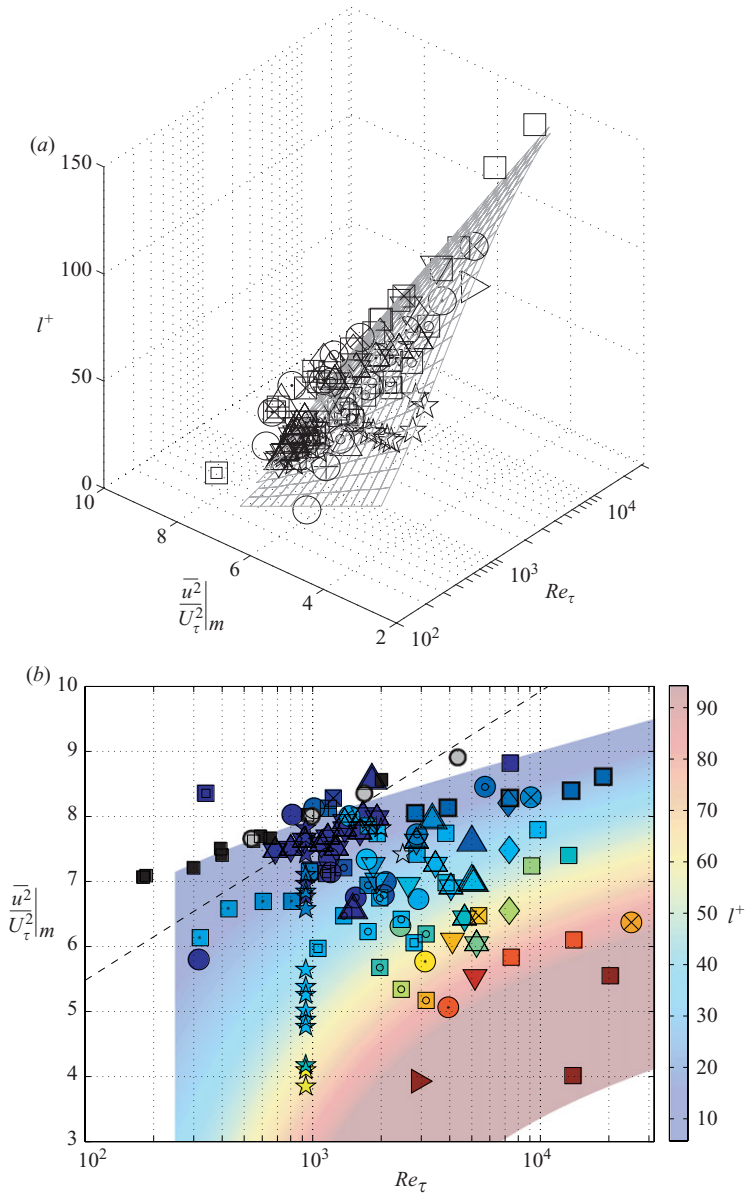
FIGURE 2. Variation of the peak value of the inner-scaled streamwise turbulence intensity with the Reynolds number and l^+ for various experiments: (a) on three-dimensional axis; (b) with symbols coloured according to l^+ (see colour scale). See figure 1 for symbol key. Transparent coloured surface in background shows (3.1) evaluated over data range; ■ shows DNS data of Moser, Kim & Mansour (1999), Iwamoto, Suzuki & Kasagi (2002) and del Álamo *et al.* (2004); ● shows LDV data of DeGraaff & Eaton (2000). The dashed line shows the similarity formulation of Marusic & Kunkel (2003) ($1.036 + 0.965 \log_e Re_\tau$). Square symbols with bold outline show the matched l^+ Melbourne data.

is in the range $3 \lesssim \Delta y^+ \lesssim 6$. It can be seen that these data follow quite well the edge of the coloured surface (which is (3.1) evaluated at $l^+ = 3$). However, the DNS data seem to exhibit a slightly stronger growth in the peak intensity with Re_τ. It must be cautioned that some of these channel-flow simulations will be subject to

pressure gradient effects (since the viscous-scaled streamwise pressure gradient p_x^+ becomes significant at low Reynolds numbers; see Nickels 2004). The LDV data of DeGraaff & Eaton (2000) are also included in figure 2(*b*) as the solid grey symbols. Again, although these data are close to the edge of the coloured surface, the rise with Reynolds number seems marginally steeper than the general hot-wire-measured trend. The measurement volume quoted by DeGraaff & Eaton (2000) for these LDV measurements is $60 \times 35\,\mu m$ in y and z respectively. For the Reynolds numbers shown in figure 2(*b*) this ranges from approximately 1×0.6 to 7.5×4.4 wall units (although it is debateable whether spatial averaging can really be assumed over an LDV measurement volume). The dashed line in figure 2(*b*) shows $\overline{u^2}/U_\tau^2|_m$ as predicted by the similarity formulation of Marusic & Kunkel (2003), a simplified form of which is given in Hutchins & Marusic (2007*a*). The lack of agreement between this curve and the surface described by (3.1), and also the DNS and LDV data, might suggest that the empirical constants used for these similarity approximations require adjustment.

In simple terms, figure 2 and the accompanying surface (3.1) show that the near-wall peak in turbulence intensity is subject to two competing effects. Whilst it will tend to rise with the Reynolds number, the measured value will drop with increasing l^+. For most facilities, if wire length l is fixed, this implies an approximately constant l/δ. (This statement is exact for fully developed internal flows and, assuming a fixed streamwise location, can be considered approximately true for external flows.) Thus as an approximation we can state that l^+ increases approximately linearly with Re_τ:

$$l^+ = \frac{l}{\delta}\frac{\delta U_\tau}{\nu} \propto Re_\tau. \tag{3.2}$$

This can explain the numerous studies (e.g. Mochizuki & Nieuwstadt 1996; Durst *et al.* 1998) that have reported no growth in $\overline{u^2}/U_\tau^2|_m$ with Reynolds number. Rearranging the surface fit of (3.1) we can obtain an expression for the variation in l^+ with Re_τ that would be necessary to record a constant near-wall peak (E):

$$l^+ = \frac{A\log_{10}Re_\tau + D - E}{B + C/Re_\tau}. \tag{3.3}$$

As an example, figure 3 shows l^+ against Reynolds number for all zero-pressure-gradient turbulent-boundary-layer data considered by Mochizuki & Nieuwstadt (1996, who found no Re dependence for the near-wall peak). The solid line shows (3.2) evaluated for $l/\delta = 0.01$. The data are scattered, but in general the data used by Mochizuki & Nieuwstadt (1996) exhibit an approximately linear growth with Re_τ. The dashed line shows (3.3) evaluated for $E = 2.7^2$ (the approximate constant proposed by their study). Clearly the data they have considered exhibit a growth in l^+ with Re_τ, which is very close to that required to give constant $\overline{u^2}/U_\tau^2|_m$. Hence it is easy to understand how researchers have in the past arrived at the erroneous conclusion that the near-wall peak in turbulence intensity (when scaled with U_τ) is independent of Re_τ.

3.2. *Is $l^+ = 20$ small enough?*

One of the key recommendations from LB87 is that l^+ should be less than 20. This stems from their assertion in the abstract that 'the turbulence intensity, flatness factor and skewness factor of the longitudinal velocity fluctuations are nearly independent of wire length when the latter is less than 20–25 wall units.' In this section we reassess this remark in light of the available data. The data in LB87 are presented in a way such that the effects of l^+ are somewhat blurred within the effects of l/d
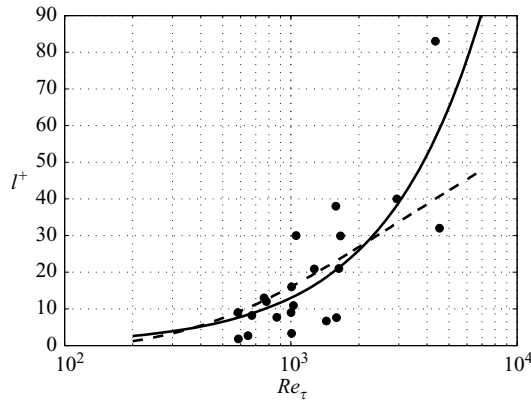
FIGURE 3. The variation of l^+ with the Reynolds number ($\bullet$) for the zero-pressure-gradient turbulent-boundary-layer data considered by Mochizuki & Nieuwstadt (1996). The solid line shows the linear relation (3.2) evaluated for $l/\delta = 0.01$. The dashed line shows (3.3) evaluated at $E = 2.7^2$.
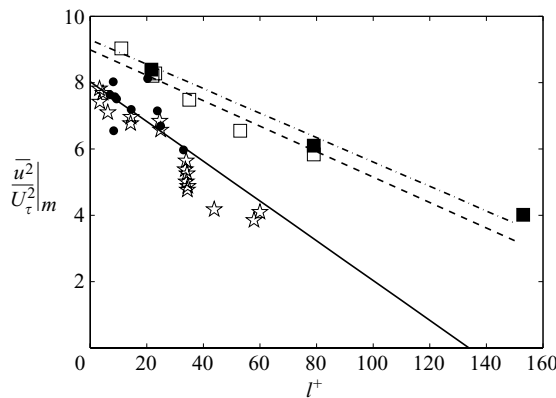

FIGURE 4. Dependence of near-wall peak ($\overline{u^2}/U_\tau^2|_m$) on l^+ for selected Reynolds numbers and with $l/d > 200$ ($\star$) (LB87) at $Re_\tau \sim 1000$; $\bullet$, other data from figure 1 in which $800 < Re_\tau < 1100$; $\square$, current study and Nickels *et al.* (2007) at $Re_\tau \approx 7300$; $\blacksquare$, current study at $Re_\tau \approx 14\,000$. The solid, dashed and dot-dashed lines show (3.1) evaluated at $Re_\tau = 1000$, 7300 and 14\,000 respectively.

(both of which were varied during experiments). To clarify this, figure 4 replots as pentagram symbols only those data of LB87 for which $l/d > 200$. (The effect of l/d is considered in more detail in § 7; for now we stick to the conclusion of LB87 that l/d should exceed 200 for accurate measurements.) The dots in figure 4 show all other data compiled in figure 1 for which $800 < Re_\tau < 1100$ (Purtell, Klebanoff & Buckley 1981; Balint, Wallace & Vukoslavčević 1991; Erm & Joubert 1991; Österlund 1999; Hutchins & Marusic 2007b). The accompanying solid line shows (3.1) evaluated at comparable *Re*. Obviously the data exhibit scatter, yet in general we can see that the error caused by using a wire of length $l^+ = 20$ is significant as compared to an ideal wire of infinitely small size ($l^+ \to 0$). LB87 have stated that the measured intensity $\sqrt{\overline{u^2}}/U_\tau|_m$ changes by 4 % for $l^+ < 20$–25. However the raw data of LB87

in figure 4 and accompanying fit from (3.1) might imply that this error is optimistic. Data from the HRNBLWT at $Re_\tau \approx 7300$ and $14\,000$ are also shown in figure 4 by the open and solid squares respectively. (The dashed and dot-dashed lines show (3.1) evaluated at the respective Re.) It is clear in general that as we move to higher Re, the percentage attenuation in the near-wall peak due to finite wire-length effects reduces. The percentage error predicted from (3.1) due to a wire of length $l^+ = 20$ compared to an ideal wire ($l^+ \to 0$) is given by

$$|\% \text{ error}|_{l^+=20} = 100 \times \frac{20\,(B + C/Re_\tau)}{(A \log_{10} Re_\tau + D)}. \tag{3.4}$$

The absolute peak error is given by the numerator of (3.4) and will tend towards a constant value as Re_τ becomes large (i.e. as the l/δ term of (3.1) tends to zero). This behaviour is later confirmed from decomposed signals in §4.1. However, the fall in percentage error with Re will continue indefinitely (since the denominator of (3.4) increases as the logarithm of Re_τ). It will be shown in the following sections that this is due to an increasing presence of large-scale fluctuations in the near-wall region as the Reynolds number increases. Thus at elevated Re_τ the small-scale fluctuations amount to a decreasing proportion of the total broadband intensity at the location of the near-wall peak, and hence percentage attenuation due to a given l^+ will reduce (see Hutchins & Marusic 2007*b,a* and §4.1.1).

3.3. *Issues related to the fitted surface*

Though the surface described by (3.1) does a reasonable job at mapping the distribution of experimental data, some scatter still remains. Aside from l^+ and Re_τ, there are many other factors in hot-wire anemometry experiments that could potentially influence $\overline{u^2}/U_\tau^2|_m$.

3.3.1. *Experimental error*

There are numerous sources of experimental error with hot-wire operation, all of which can lead to errors in velocity measurements, turbulence intensities and, where Clauser charts are employed, friction velocity U_τ. These include (but are not limited to) drift in ambient conditions such as temperature (e.g. Cimbala & Park 1990), humidity (e.g. Durst *et al.* 1996) and pressure drift (e.g. Nekrasov & Savostenko 1991); problems with wire degradation such as change in material properties due to incomplete cleaning (Willmarth & Bogar 1977), electromigration (see Willmarth & Sharma 1984) and wire fouling (Wyatt 1953); and wider problems with the facility such as pressure gradients (Fernholz & Warnack 1998) and elevated free-stream intensities (Hancock & Bradshaw 1989; Barrett & Hollingsworth 2003; Stefes & Fernholz 2004). Many of the data included in figures 1 and 2 use U_τ values obtained using the Clauser method (see §2.4 for a description of the errors associated with this technique). Ong & Wallace (1998) have pointed out that at low Reynolds numbers, the Clauser method can systematically overestimate U_τ (as compared to the near-wall velocity gradient). Consequently, the recorded values of $\overline{u^2}/U_\tau^2|_m$ at low Reynolds numbers in figures 1 and 2 could be strongly effected by this type of error.

3.3.2. *Internal and external geometries*

For the data considered here, no attempt has been made to differentiate between internal and external geometries. It is possible that $\overline{u^2}/U_\tau^2|_m$ and its Reynolds-number dependence could be different for pipes and channels than for boundary layers. Certainly there is growing evidence that the largest scale structures in the logarithmic and wake regions of internal flows are different from those of flat-plate boundary

layers. Through analysis of premultiplied spectra ($k_x\phi_{uu}$, where k_x is the streamwise wavenumber and ϕ_{uu} is the energy spectrum of streamwise velocity fluctuations), Kim & Adrian (1999) have reported length scales of up to 14 pipe radii in pipe flows. This is in contrast to peak length scales of 6δ found from similar measurements in boundary layers by Hutchins & Marusic (2007a). By comparing the log-region peak in $k_y\phi_{uu}$ (where k_y is the spanwise wavenumber) between channel DNS and boundary-layer experiments (Tomkins & Adrian 2003; Abe *et al.* 2004; Kasagi *et al.* 2005), Hutchins & Marusic (2007b) have noted that the widths of the large-scale structures in internal geometries are larger than those in boundary layers (by a factor of approximately 1.6). Recently, Monty *et al.* (2007) have reiterated this tendency through analysis of experimental channel and pipe correlations (see also Bailey *et al.* 2008). Since the growth in $\overline{u^2}/U_\tau^2|_m$ with Reynolds number is due in some part to the footprint imposed by the largest scales on to the near-wall region (Hutchins & Marusic 2007a) and since these largest scales clearly differ between internal and external flows, it is possible that, with sufficient data, it may be necessary to fit a different surface (of the type shown by equation 3.1) to pipe and channel flows than to flat-plate boundary layers.

3.3.3. *Temporal resolution*

Temporal resolution limits, imposed by the anemometry or any Nyquist filtering, can cause additional attenuation of measured turbulent energy. See §8 for a full discussion of this phenomenon.

3.3.4. *Lack of high-Reynolds-number data*

The surface fit is also somewhat handicapped by a lack of reliable high-Reynolds-number data. This is exacerbated by the fact that high-*Re* data tend to be attained using larger l^+ (see (3.2)). It would be dangerous to extrapolate this fit beyond the limits shown in figure 2.

4. The 'outer hump' in broadband streamwise intensity: is it real?

It is not only the near-wall peak in $\overline{u^2}/U_\tau^2$ that is effected by the hot-wire length. Figure 5(a) shows profiles of streamwise turbulent intensity for several viscous-scaled wire lengths at $Re_\tau \approx 14\,000$. As l^+ increases from 22 to 79, the near-wall peak is diminished, and a secondary peak emerges in the log region of the $\overline{u^2}/U_\tau^2$ profile. When l^+ is increased still further, the near-wall peak disappears entirely, and the log-region peak begins to fall in magnitude. It is also noted that the location of any apparent outer hump seems to shift to higher z^+ as l^+ is increased. Figure 5(b) shows the associated mean velocity profiles. Note that within the accuracy of hot-wire measurements, the mean velocity profiles show no systematic variation with l^+.

4.1. *Decomposed turbulence intensities*

We can obtain a clearer picture of the effects of spatial resolution on the broadband turbulence intensity by decomposing the fluctuating velocity signals into a small-scale (where $\lambda_x^+ < 7000$) and a large-scale (where $\lambda_x^+ > 7000$) contribution. For this we use a simple cutoff spectral filter. The value $\lambda_x^+ = 7000$ is chosen after Hutchins & Marusic 2007b; λ_x is the streamwise wavelength of (Fourier-decomposed) fluctuations, defined as $2\pi/k_x$, where k_x is streamwise wavenumber. By integrating the surface above and below this line we can decompose the broadband turbulence intensity into a small- and a large-scale contribution. Figure 6 shows the resulting contributions for the wires of various l^+. Symbols are as given in figure 5, with the solid symbols showing the
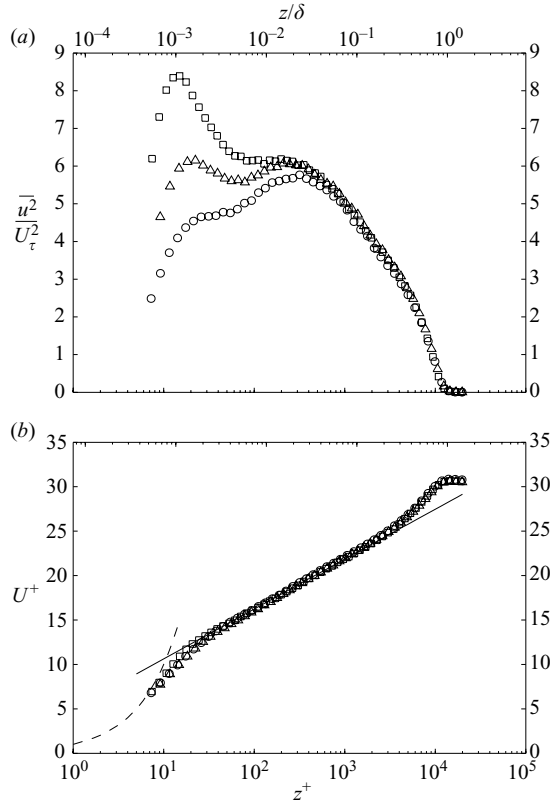
FIGURE 5. (a) Broadband turbulence intensity profiles in a fully developed turbulent boundary layer at $Re_\tau \approx 14\,000$ using three different wire lengths. (b) Associated mean velocity profiles: $\square$, $l^+ = 22$ ($l/d = 200$); $\triangle$, $l^+ = 79$ ($l/d \approx 360$); $\bigcirc$, $l^+ = 153$ ($l/d \approx 700$). The solid line shows $U^+ = (1/\kappa) \ln(z^+) + A$ (where $\kappa = 0.41$ and $A = 5.0$). The dashed line shows $u^+ = z^+$.
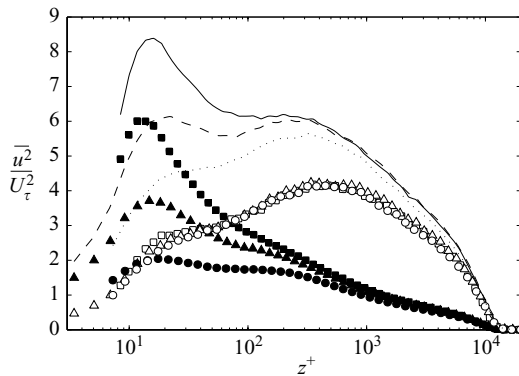

FIGURE 6. Turbulence intensity profiles decomposed into small-scale ($\lambda_x^+ < 7000$, solid symbols) and large-scale components ($\lambda_x^+ > 7000$, open symbols). The symbols show different l^+ as given in figures 5 and 6. The lines show sum of small- and large-scale components for $l^+ = 22$ (solid line), $l^+ = 79$ (dashed line) and $l^+ = 153$ (dotted line).

small-scale contribution and the open symbols showing the large-scale contribution. Note that the small- and large-scale contributions for a given l^+ sum to give the broadband intensity shown in figure 5 (shown by the lines in figure 6). Though the
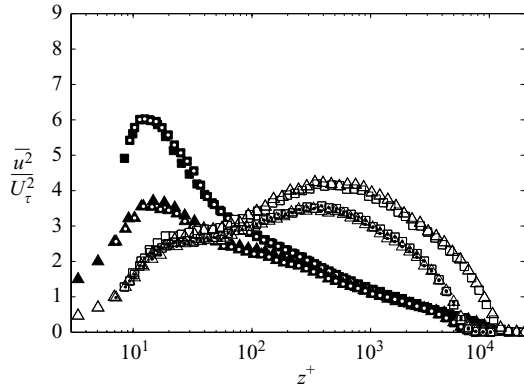
FIGURE 7. Turbulence intensity profiles decomposed into small-scale ($\lambda_x^+ < 7000$, solid symbols) and large-scale components ($\lambda_x^+ > 7000$, open symbols) for two different Reynolds numbers. The dotted symbols ($\triangle$, $\square$) show $Re_\tau \approx 7300$. The plain symbols ($\triangle$, $\square$) show $Re_\tau \approx 14\,000$. The triangular symbols ($\triangle$, $\triangle$) show $l^+ = 79$. The square symbols ($\square$, $\square$) show $l^+ = 22$.

division is somewhat arbitrary and abrupt, the decomposed statistics are a useful metric for understanding the broadband intensity, which we can consider to be the sum of two competing modes: a small viscous-scaled component primarily located in the near-wall region and a larger outer-scaled component peaking in the log region. There is considerable overlap between these modes, with the large scale extending down to the wall and a diminishing small scale influence penetrating to the edge of the boundary layer.

As l^+ increases, figure 6 shows that the measured small-scale energy is diminished. The collapse of all open symbols, on the other hand, indicates that the large-scale contribution remains approximately the same over the range of l^+ considered. (Even the longest wire at $l^+ = 153$ only has $l/\delta \approx 0.01$.) Thus as l^+ increases, we are increasingly sensing only the large-scale contribution to the broadband intensity. Eventually this will result in a 'double hump' in the spatially under-resolved broadband intensity, ultimately giving way to the single outer hump with larger l^+. Both of these phenomena should just be considered as symptoms of the filtering of small-scale fluctuations from the signal (and the subsequent uncovering of the large-scale mode). The key point to note here is that small-scale energy extends a considerable distance from the wall. Thus the spatial filtering due to largest wire length is evident in the broadband intensity profile deep into the log region. (There is spatial filtering up to beyond $z^+ = 1000$ for $l^+ = 153$.)

It is important to note that although we show here that there is no outer hump for spatially well-resolved data up to $Re_\tau = 18\,830$ (see §4.3) and that within this limit such a hump can only be present due to poor experimental resolution, this should not necessarily preclude the possibility that at higher Reynolds numbers a legitimate outer peak could emerge in the broadband intensity that is not resolution related.

4.1.1. *Reynolds-number effects*

Figure 7 shows similarly decomposed intensities for two different Reynolds numbers and with two matched viscous-scaled wire lengths. In this case it is noted that the small-scale contributions (solid symbols) collapse down on to two distinct curves, dependant only on viscous-scaled wire length l^+ and independent of the Reynolds

number. In other words, the $l^+ = 22$ wire records the same viscous-scaled small-scale contribution regardless of the Reynolds number (solid square symbols). The same is also true of the small-scale fluctuations measured by the $l^+ = 79$ wire (solid triangular symbols). However, the opposite is true of the large-scale contribution. The large-scale contribution (at a given Re) is effectively independent of l^+ as shown by figure 6 (provided l/δ is small). However, as Re_τ increases, figure 7 shows a very clear increase in the large-scale contribution to intensity. This effect is important, since it explains the form of the surface fit (3.1), particularly the decreasing percentage attenuation due to a given l^+ discussed in §3.2 and shown by (3.4). Figure 7 seems to show that the small-scale contribution is invariant with the Reynolds number, depending only on the viscous-scaled wire length. However, as the Reynolds number increases an ever-increasing large-scale contribution is present in the near-wall region. Thus at elevated Re_τ the small-scale fluctuations amount to a decreasing proportion of the total broadband intensity, and hence percentage attenuation due to a given l^+ (at a fixed z^+) will reduce with Reynolds number.

It must be cautioned that this can only be considered true with sufficiently high Reynolds number (sufficient separation of scales). At low Reynolds numbers, a large l^+ will also be large in terms of l/δ and hence would be expected to attenuate some of the large outer-scaled (δ-scaled) energy (see term 3 in (3.1)). Indeed as the Reynolds number is reduced, the small-scale contributions defined by the crude spectral filter $\lambda_x^+ < 7000$ will increasingly contain large outer-scaled contributions (see figure 3 of Hutchins & Marusic 2007*b*).

4.2. *The premultiplied energy spectra*

The secondary outer hump exhibited by the spatially under-resolved intensities can be explained through consideration of the energy spectra at each wall-normal position across the boundary layer. This is shown for the three different wire lengths in figure 8. These figures are formed by plotting isocontours through the surface constructed from the one-dimensional premultiplied energy spectra of u fluctuations at each wall-normal z position. This type of energy map is introduced and studied in detail in Hutchins & Marusic (2007*a,b*). In these studies it was shown that with high enough Re, the energy map has two clear energetic peaks. The peak closest to the wall has a location fixed in viscous-wall units (at $\lambda_x^+ = 1000$, $z^+ = 15$) and has been termed the 'inner site', representing energetic contributions due to the near-wall cycle. The second peak occurs in the logarithmic region and has been termed the 'outer site', with a location nominally fixed in outer units at $\lambda_x \approx 6\delta$, $z \approx 0.06\delta$. (Recently Mathis, Hutchins & Marusic 2009 revised slightly these estimates over a larger range of Reynolds numbers.) It was suggested by Hutchins & Marusic (2007*a*) that this outer site might be the contribution due to the very long meandering features found to populate the log region (and termed 'superstructures'). The location of these two peaks are shown by the + symbols in figure 8. The most resolved energy map of figure 8(*a*) clearly exhibits these two energetic peaks. As l^+ is increased, figure 8(*b,c*) demonstrates that the fluctuating energy due to the near-wall cycle is increasingly under-resolved, and the inner site starts to disappear. In addition to this, the measured small-scale energy due to the attached eddies is also diminished by the longer wires. This region is labelled in figure 8(*a*) and is visible in the energy map as inclined contours in which the length scale λ_x scales with distance from the wall (i.e. $\lambda_x \propto z$). Attenuation in this region is highlighted by the dashed contour in plots (*b*) and (*c*) which show the $k_x\phi_{uu}/U_\tau^2 = 0.2$ contour for the shortest wire ($l^+ = 22$). As was noted
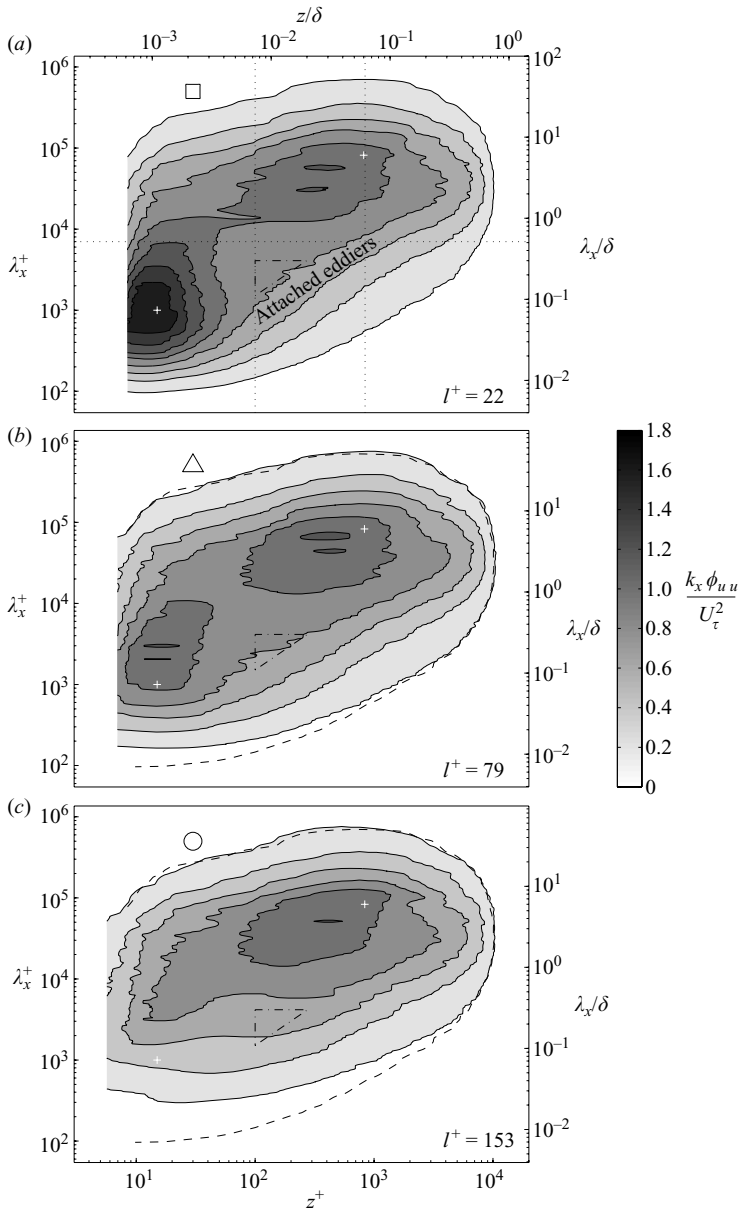
FIGURE 8. Contour maps showing variation of one-dimensional premultiplied spectra with wall-normal position at $Re_\tau \approx 14\,000$ for (a) $l^+ = 22$, (b) $l^+ = 79$ and (c) $l^+ = 153$. The contours are from $k_x\phi_{uu}/U_\tau^2 = 0.2$–1.8 in steps of 0.2. The dashed contours in (b) and (c) show $k_x\phi_{uu}/U_\tau^2 = 0.2$ for $l^+ = 22$. The symbols adjacent to the label refer to the data in figure 5(a); + symbols show the location of inner ($\lambda_x^+ = 1000$, $z^+ = 15$) and outer ($\lambda_x = 6\delta$, $z = 0.06\delta$) energy sites as defined in Hutchins & Marusic (2007a). The dot-dashed triangular region shows the location of the k_x^{-1} plateau as given by Nickels *et al.* (2005).

previously for figure 6, the effects of spatial resolution are not merely confined to the near-wall region.

To highlight this point, figure 9 shows the missing inner-scaled premultiplied energy (χ) for (a) $l^+ = 79$ and (b) $l^+ = 153$ as an absolute reduction compared to that
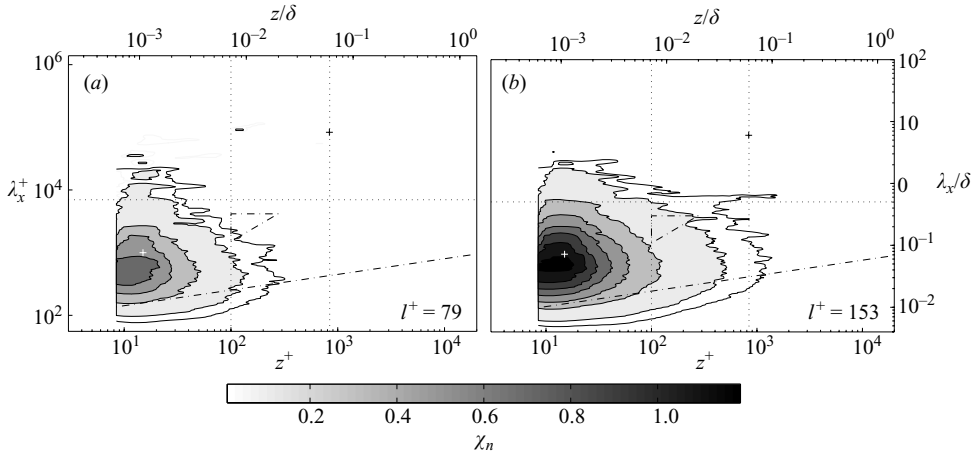
FIGURE 9. Missing energy χ for (a) $l^+ = 79$ and (b) $l^+ = 153$. The dashed lines show $z = 10l$. The horizontal dotted line shows $\lambda_x^+ = 7000$. The vertical dotted lines show $z^+ = 100$ and $z/\delta = 0.06$. The dot-dashed triangular region shows the location of the k_x^{-1} plateau as given by Nickels *et al.* (2005); + symbols show inner and outer energetic sites. The dot-dashed inclined line shows $100(\kappa z^+)^{1/4}$.

measured by the $l^+ \approx 22$ wire:

$$\chi_n = \frac{k_x(|\phi_{uu}(\lambda_x, z)|_{l^+=22} - |\phi_{uu}(\lambda_x, z)|_{l^+=n})}{U_\tau^2}. \tag{4.1}$$

Together these plots indicate that spatial resolution issues can lead to substantial errors for standard premultiplied energy spectra and that these errors can extend a considerable distance beyond the immediate near-wall region. As discussed previously, energy maps of this type are subject to complicated scaling, with a near-wall peak scaling on viscous units, an outer-peak scaling on boundary-layer thickness and an attached region scaling on distance from the wall z. It is thus unlikely that we can reliably state a height (z_{min}) above which spatial resolution errors will be negligible. In the past such attempts have been made (usually attempting to describe z_{min} as a linear function of wire length). However, figure 9 would suggest that this approach will not work. The lowest contour, drawn at $\chi_n = 0.05$, extends to approximately $z/l \approx 4$ for the $l^+ = 79$ data. For the $l^+ = 153$ wire, however, there are signs of spatial attenuation to at least $z/l = 9$.

4.3. *The HRNBLWT data with matched l^+*

Figure 10(a) shows the inner-scaled streamwise turbulence intensity profiles for all Reynolds numbers measured in the HRNBLWT in which the inner-scaled wire length was approximately constant ($l^+ \approx 22$). When viewed over this Reynolds-number range ($2820 < Re_\tau < 18\,830$) the growing large-scale contribution is clear, even from the broadband result. The fact that this growing large-scale contribution extends down to the wall leads to a steady growth in the magnitude of the near-wall peak ($\overline{u^2}/U_\tau^2|_m$) with Reynolds number (see also the bold square symbols in figure 2b). The important point to note here is that up to $Re_\tau = 18\,830$, there is no outer peak in the broadband intensity for spatially well-resolved measurements ($l^+ \lesssim 20$) in the HRNBLWT. At these Reynolds numbers, an outer peak can only be produced through attenuation of certain turbulent scales due to large l^+ ($\gtrsim 50$–60). As an example of this figure 10(b)
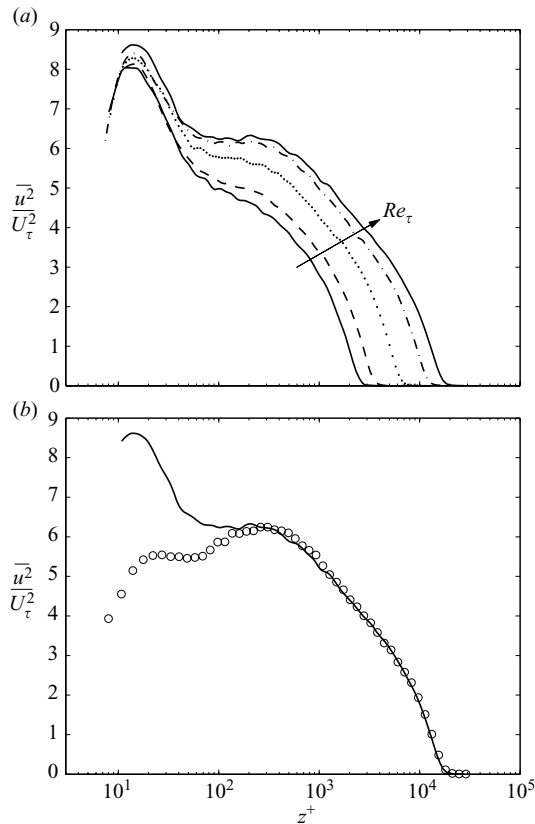
FIGURE 10. Turbulence intensity profiles (*a*) for all HRNBLWT profiles with matched $l^+ \approx 22$ at $Re_\tau = 2820, 3910, 7340, 13\,620, 18\,830$; (*b*) a comparison of the HRNBLWT data at $Re_\tau = 18\,830$, $l^+ = 22$ (solid line) with the HRNBLWT data at $Re = 20\,390$, $l^+ = 115$ (○).

shows a comparison of the well-resolved HRNBLWT data ($Re_\tau = 18\,830$, $l^+ = 22$) with a profile taken with a larger wire ($l^+ = 115$, shown by the circles) at similar Reynolds numbers. The resulting profile, in which the near-wall peak is completely absent leaving just an outer hump, is remarkably similar to the result from the Princeton superpipe at similar Reynolds numbers ($Re_\tau = 19\,700$; Morrison *et al.* 2004). Note however that a slightly longer wire is required in the HRNBLWT to obtain a similar broadband intensity profile ($l^+ = 115$ for the HRNBLWT as compared to $l^+ = 76$ for the superpipe). It is important to remain open to the fact that differences may exist in the broadband intensity profiles for flat-plate boundary layers and internal geometries (such as pipes and channel flows). The energy spectra exhibit clear differences across the log regions of internal and external geometries (see §3.3.2), and it would not be unreasonable to assume that this could extend to subtle differences in broadband profiles. Ultimately, verification of this will have to await the availability of other high-Reynolds-number pipe or channel-flow results (or new superpipe measurements when smaller probes with more suitable l/d and l^+ become available).

5. A closer look at k_x^{-1} scaling

The attenuation of energy due to wire length detailed in figures 8 and 9 offers clear insight into the seemingly contentious issue of k_x^{-1} scaling. Such a region of

self-similar scaling is predicted by the attached eddy model of Perry & Chong (1982) and by scaling and overlap arguments (detailed most recently by Nickels *et al.* 2005, 2007). Nickels *et al.* (2005) found clear regions of k_x^{-1} energy in experimental data at $Re_\tau \approx 15\,000$. These regions were shown to scale with both inner and outer scalings and hence are self-similar. However, other high-Reynolds-number studies have failed to find such behaviour and have argued against its existence. Whether or not k_x^{-1} scaling exists, we can show here that the energy spectra within the mooted k_x^{-1} region is substantially effected by l^+. As an example, Nickels *et al.* (2005) have predicted that a k_x^{-1} region will appear in the u spectra within the limits $k_x \delta > 21$ and $k_x z < 0.4$ for $z^+ > 100$. Hence from these limits one can deduce that a k_x^{-1} region is only likely to be present in the range of wall distances in which $100 < z^+ < 2Re_\tau/105$. The k_x^{-1} region (based on the limits of Nickels *et al.* 2005) is drawn in figures 8 and 9 by the dot-dashed lines (showing $\lambda_x^+ < 2\pi Re_\tau/21$, $\lambda_x^+ > 2\pi z^+/0.4$ and $z^+ > 100$). The vertices of this triangular region are given by the (z^+, λ_x^+) coordinates: $(100, 500\pi)$, $(2Re_\tau/105, 2\pi Re_\tau/21)$ and $(100, 2\pi Re_\tau/21)$. Based on these empirical limits the k_x^{-1} region will only exist where $Re_\tau > 5250$. With the premultiplication shown in figure 8 any k_x^{-1} scaling would appear as a plateau within the triangular dot-dashed region describing these limits. Whilst this is true for the most spatially resolved case of figure 8(*a*), with the triangular region seeming to enclose a constant contour value (constant grey shading), the spectra as measured with larger wires (figure 8*b,c*) show this region to lie within a highly attenuated, sloping, region of the energy map. Although, the choice of contour levels can effect the view from figure 8, it is clear that the triangular region lies within a flatter or more plateau-like region for the smallest wire of figure 8(*a*). Attenuation of the expected k_x^{-1} region is also obvious for the missing energy maps of figure 9. As wire length increases the triangular plateau region of expected k_x^{-1} behaviour is increasingly eroded by attenuation owing to spatial resolution. Thus what ought to be a plateau in figure 8(*a*) becomes a gradient.

This eroding of the k_x^{-1} region due to wire length is shown in a more traditional format in figure 11(*a*), which shows premultiplied inner-scaled streamwise energy at $z^+ = 100$ (corresponding to the vertical dotted lines in figures 8 and 9). Note that for this figure we use wavenumber (k_x) rather than wavelength $(\lambda_x = 2\pi/k_x)$ for consistency with Morrison *et al.* (2004) and Nickels *et al.* (2005). Clearly the k_x^{-1} plateau, evident with $l^+ = 22$ (and evident at similar Reynolds numbers from Nickels *et al.* 2005), is not present at all with $l^+ = 79$ and 153, as the longer wires increasingly attenuate the smallest scales. Figure 11(*b*) shows premultiplied spectra at $z^+ = 840$, corresponding to the location of the outer energetic site ($0.06Re_\tau$). These spectra are measured at locations at which $z^+ > 2Re_\tau/105$ and hence have no plateau, a fact consistent with the limits derived by Nickels *et al.* (2005). Note that in this instance the signs of attenuation due to wire length are less acute, with only the $l^+ = 153$ wire exhibiting attenuation in the range $0.0013 < k_x^+ < 0.04$ (as predicted by the missing energy plots in figure 9, where $z^+ = 840$ is shown by the vertical dotted line).

Whether or not one subscribes to the hypothesis underpinning self-similarity and k_x^{-1} scaling, it is clear from Nickels *et al.* (2005) and figures 8(*a*) and 11(*a*) that a plateau-like region exists in the premultiplied energy spectra when the flow is sufficiently spatially resolved. Figure 11 shows that as l^+ increases this plateau-like region is increasingly eroded.

Figure 11 could explain the lack of a k_x^{-1} scaling noted in the inner-scaled spectra of Morrison *et al.* (2004), where spectra were shown for $Re_\tau = 1500$ and 10^6. The lowest Reynolds number has inadequate separation of scales to see a region of self-similarity, since there is no wall-normal position for which $100 < z^+ < 2Re_\tau/105$. The highest
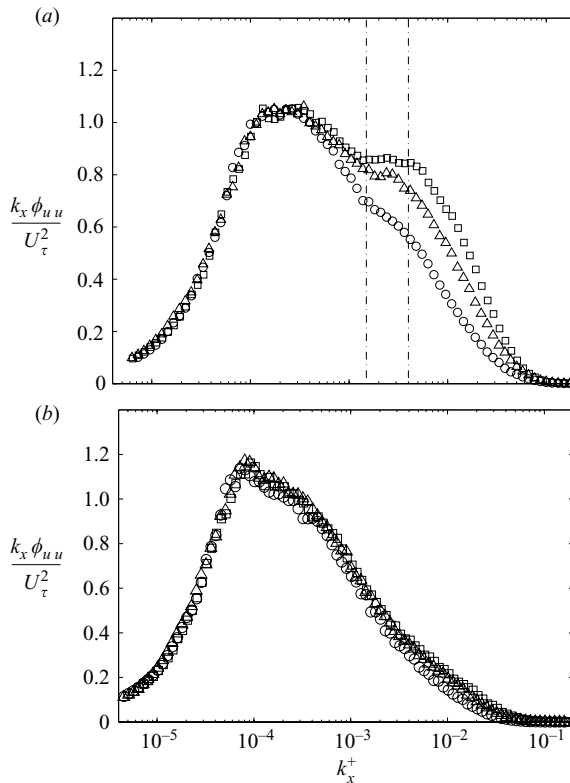
FIGURE 11. Premultiplied inner-scaled streamwise energy spectra at (a) $z^+ \approx 100$ ($z/\delta = 0.007$) and (b) $z^+ = 840$ ($z/\delta = 0.06$) for $l^+ = 22$ ($\square$), $l^+ = 79$ ($\triangle$) and $l^+ = 153$ ($\bigcirc$); $Re_\tau = 14\,000$. The dot-dashed lines in (a) enclose band of expected k_x^{-1} collapse as given by Nickels *et al.* (2005).

Reynolds number meanwhile has a wire length of $l^+ = 385$ which will severely erode the k_x^{-1} region (see figure 11a). However, it is also the case that the energy spectra in channels and pipes are different from those of turbulent boundary layers (due to differences in the largest scales; see for example Kim & Adrian 1999; Hutchins & Marusic 2007b; Monty *et al.* 2007). The approximate limits of Nickels *et al.* (2005) are for boundary layers only and may not be applicable to internal geometries.

6. Kolmogorov scales

The dot-dashed inclined lines in figure 9 show $\lambda_x^+ = 100(\kappa z^+)^{1/4}$. It is clear that these lines transect a region of substantial missing energy. Since in the log region we can approximate that $\eta^+ = (\kappa z^+)^{1/4}$, this would seem to imply that larger wires can cause spatial attenuation in the region $k_x \eta = 2\pi/100 \approx 0.06$, very close to the 'spectral bump' in the Kolmogorov-scaled energy spectra (Saddoughi & Veeravalli 1994; McKeon & Morrison 2007). To illustrate this, figure 12 shows Kolmogorov-scaled streamwise energy spectra for the three wire lengths at $z^+ = 1000$ and 2100 ($z/\delta \approx 0.07$ and 0.15). Here we use the approximation that production balances dissipation in the logarithmic region; hence $\epsilon = (U_\tau^3/\kappa z)$ and $\eta = (\nu^3/\epsilon)^{1/4}$. It is clear that spatial resolution has a large effect on these results. There is considerable attenuation occurring around the location of the 'spectral bump' (as marked by the dashed line). This bump disappears almost entirely for the longest wire. In addition, spatial resolution clearly governs
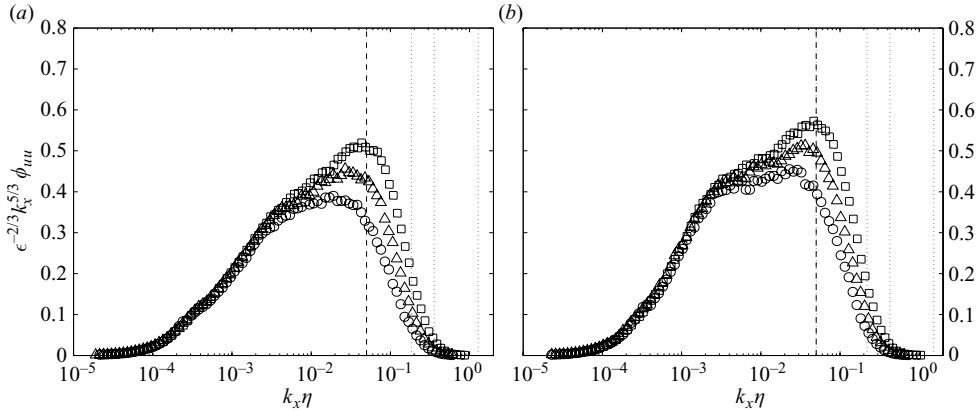
FIGURE 12. Kolmogorov-scaled energy at (*a*) $z^+ = 1000$ $z/\delta \approx 0.07$) and (*b*) $z^+ = 2100$ ($z/\delta \approx 0.15$) at $Re_\tau \approx 13\,620$ for different wire sizes, $l^+ = 22$, 79 and 153. The symbols are as given in figure 11. The dashed lines show approximate location of 'spectral bump', $k\eta = 0.05$ (Saddoughi & Veeravalli 1994; McKeon & Morrison 2007). The dotted lines show $2\pi\eta/l$ for the three wire lengths, $l^+ = 22$, 79 and 153.

the appearance of any $-5/3$ scaling region (which would appear as a horizontal line with this premultiplication), also changing the value of the apparent Kolmogorov constant.

It is perhaps not surprising that a sensor length that is greater than the Kolmogorov scale might effect the small-scale end of the spectra. However, it is crucial to note from figure 12 that these effects extend to a surprising distance from the wall. Indeed, the wire with $l^+ = 79$ exhibits substantial attenuation at $z^+ = 2100$ (even though $z/l > 26$). It is also important to recognize that attenuation due to spatial resolution reduces the energy content of wavenumbers far below that which we might assume from local isotropy. A normal hot wire of length l might be expected to attenuate structures of spanwise width l and smaller. If an assumption of isotropy is made, then we assume that these structures also have the same streamwise extent and would expect the attenuation to appear at a streamwise wavelength comparable to the length of the wire. If, however, the structures of spanwise width l are actually much longer in the streamwise direction, then their attenuation by a wire of l will lead to attenuation of streamwise wavelengths much greater than l (or at wavenumbers smaller than $k_x\eta|_{max} = 2\pi\eta/l$). This effect is seen in our results. Figure 12 suggests that the effects of spatial resolution extend at least to $2\pi\eta/30l$ for $l^+ = 79$ (and beyond for $l^+ = 153$). For the three wire lengths shown in figure 12(*a*) the l/η ratios are 4.9, 17.6 and 34 respectively for $l^+ = 22$, 79 and 153. The corresponding ratios for figure 12(*b*) are 4.1, 14.8 and 28.6.

7. The length-to-diameter ratio (l/d)

The second often-quoted recommendation from LB87 is that the length-to-diameter ratio of hot-wire sensors should exceed 200 ($l/d > 200$) in order to minimize attenuation caused by end conduction effects. This conclusion is largely based on the variation of the measured near-wall peak ($\overline{u^2}/U_\tau^2|_m$) for various l/d and l^+ values (although at just a single, relatively low, Reynolds number). The pentagram symbols in figure 13 show a compilation of measured $\overline{u^2}/U_\tau^2|_m$ versus l/d for all LB87 data where $l^+ < 10$. Though these data are scattered, the basic trend seems to approximately confirm the above conclusion. For l/d less than 200, there is a steadily increasing
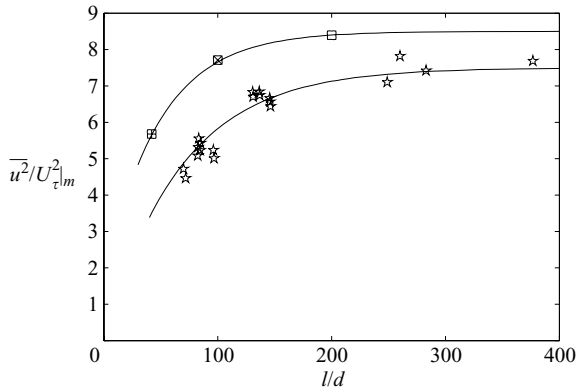
FIGURE 13. The variation of the inner-scaled near-wall peak in broadband streamwise intensity $(\overline{u^2}/U_\tau^2|_m)$ with probe length-to-diameter ratio (l/d); ☆ are from LB87, where $l^+ < 10$ and $Re_\tau \approx 1000$; the square symbols are the HRNBLWT data at $Re_\tau \approx 14\,000$ and $l/d = 200$ (□), $l/d = 100$ (⊠) and $l/d = 39$ (⊞). The solid lines show best fit to data using the form $(\overline{u^2}/U_\tau^2|_m) = B(1 - e^{A(l/d)})$.
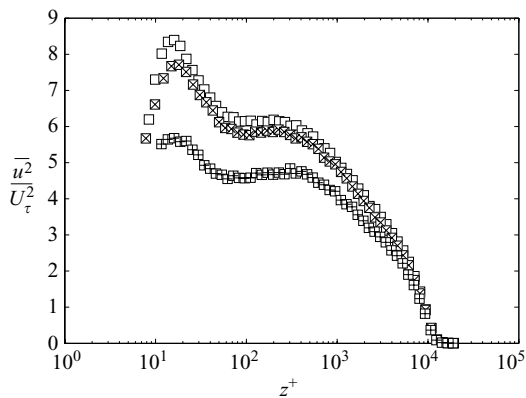

FIGURE 14. (*a*) Broadband turbulence intensity profiles in a fully developed turbulent boundary layer at $Re_\tau \approx 14\,000$ using the same wire length $l^+ \approx 22$ and with different length-to-diameter ratios, $l/d = 200$ (□), $l/d = 100$ (⊠) and $l/d = 39$ (⊞).

attenuation of the measured near-wall peak until by $l/d = 100$ this peak has been reduced by approximately 17 %. Results from the HRNBLWT reconfirm this result at higher Reynolds numbers. The square symbols in figure 13 show the corresponding HRNBLWT results at $Re_\tau \approx 14\,000$, with matched l^+ but three different l/d ratios of 200, 100 and 39. Note that all of these sensors have the same length (dimensional and viscous-scaled) with the only difference in probe geometry being the wire diameter (which is 2.5, 5 and 12.5 μm for the $l/d = 200$, 100 and 39 wires respectively). Again, these data reinforce the conclusion of LB87, showing that insufficient l/d reduces the magnitude of the measured near-wall peak. As an example, for $l/d = 100$ the measured near-wall peak at $Re_\tau \approx 14\,000$ is reduced to approximately $\overline{u^2}/U_\tau^2|_m = 7.7$ as compared to 8.4 for $l/d = 200$. The functional form (3.1) indicates that this level of attenuation is more normally associated with $l^+ \approx 33$ (when $l/d \geqslant 200$).

Unfortunately, the investigation of LB87 into length-to-diameter ratio focused solely on the effects of l/d on the near-wall peak in streamwise broadband intensity. Figure 14 expands on this view, by showing the full broadband intensity profiles

associated with the peaks discussed above. Figure 14 indicates that the effects of insufficient l/d extend far beyond the near-wall region, affecting the recorded broadband intensities throughout the boundary layer. This is an important result and would seem to indicate that insufficient l/d can cause substantial errors in measured broadband intensities, even when the distance from the wall z^+ and the wire length l^+ might otherwise suggest that the sensor is spatially resolving most of the energy. Clearly attenuation due to insufficient l/d is a quite separate issue from spatial resolution effects. Unlike attenuation due to spatial resolution, the attenuation due to insufficient l/d seems to occur at all distances from the wall and at all energetic length scales up to $\lambda_x \approx 2\delta$.

7.1. *Reynolds-number effects for l/d*

Through numerical solution of the steady-state heat-balance equation for a hot-wire filament and its support stub, Li *et al.* (2004) showed that the end conduction depends on the length-to-diameter ratio, the stub length, hot-wire material and the wire Reynolds number ($Re_w = Ud/\nu$). They defined the measure σ as the ratio of relative end conduction compared to the total heat loss from the wire (forced convection to the fluid plus end conduction). Based on the measurements of Champagne, Sleicher & Wehrmann (1967), Li *et al.* (2004) suggested the baseline $\sigma \lesssim 7\%$ as a design parameter for hot-wire probes. With this established they were able to recommend, for a given wire material, stub geometry and Reynolds number, the necessary l/d for 'accurate measurements', and simplified expressions are provided to aid in this. As a cautionary note, though the choice of $\sigma \lesssim 7\%$ can be made to yield $l/d \sim 200$ in keeping with LB87 (although only with appropriate choice of stub length, wire material, Reynolds number and the like), its choice should be viewed as somewhat arbitrary. Nonetheless, the work of Li *et al.* (2004) is very useful in demonstrating that the appropriate choice of l/d is dependent on many factors of probe geometry and more importantly Re_w. Their results clearly indicate that a lower l/d ratio (than that recommended by LB87) should be permissible at higher wire Reynolds numbers. The data of LB87 shown in figure 13 have a wire Reynolds-number range $0.2 \lesssim Re_w \lesssim 1.8$. For the HRNBLWT data in figures 13 and 14, the $l/d = 200$ wire has $1.3 \lesssim Re_w \lesssim 3.3$ across the boundary layer (from $15 < z^+ < 14\,000$), whilst the $l/d = 100$ wire has $2.7 \lesssim Re_w \lesssim 6.7$ and the $l/d = 41$ wire $5.7 \lesssim Re_w \lesssim 15.7$. Thus the results in §7 can only really prove the lack of suitability of $l/d \lesssim 200$ within this Re_w range. However, although figure 12 certainly shows that the degree of attenuation between $l/d = 200$ and $l/d = 100$ does reduce somewhat with Reynolds number, the suggestion is that this change is only a very weak function of Reynolds number.

Ultimately these issues will not be resolved until an in-depth experimental study is conducted, in which a number of full broadband intensity profiles are presented at a wide range of l/d and Re_w. Such a study would be complex, requiring a large selection of wire diameters. Complications arise, since in order to maintain constant l^+, Re_w will increase as l/d is reduced (which is true of the data in figure 13). In the interim, figures 13 and 14 would seem to suggest that it is prudent to maintain the length-to-diameter ratio at the level suggested by LB87.

8. Temporal resolution

In considering the effects of resolution we have thus far restricted our treatment to just the spatial attenuation owing to hot-wire length l. However, there is also
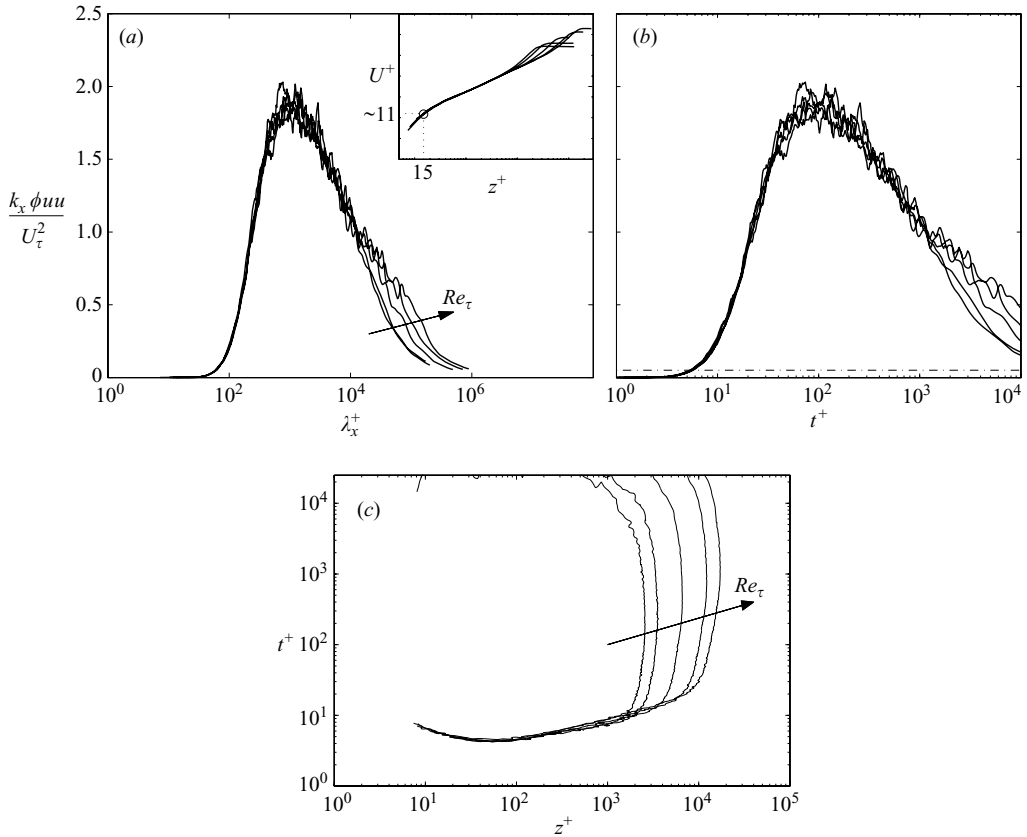
FIGURE 15. Premultiplied energy spectra of u fluctuations for $Re_\tau = 2820, 3910, 7340, 13\,620,$ $18\,830$ with $l^+ \approx 22$ (a) at $z^+ = 15$ as a function of viscous-scaled length scale λ_x^+ (the inset shows corresponding viscous-scaled mean velocity profiles) and (b) at $z^+ = 15$ as a function of viscous-scaled time scale t^+. The horizontal dot-dashed line shows $k_x \phi_{uu}^+ = 0.05$. (c) The contours of $k_x \phi_{uu}^+ = 0.05$ for the various Reynolds numbers as functions z^+ and t^+.

an effective temporal resolution imposed by the experimental set-up, which will be discussed briefly here. The temporal and spatial resolution requirements are intimately related through Taylor's hypothesis. To avoid attenuation, the spatial length of a single normal hot wire must be sufficiently small to resolve energetic scales of a given spanwise width. In much the same manner, the overall temporal resolution of a measurement system must also be sufficiently fast to resolve a structure of a given streamwise length as it advects past the sensor (at a given convection velocity). The actual relationship is complicated, since it depends on details of the flow structure, which in many instances cannot be considered isotropic. However, in general it should be obvious that in fast, high-Reynolds-number flows, the temporal resolution needs to be increased (as the convection velocity increases and the size of the smallest scales reduces).

8.1. *A maximum flow frequency*

First we will demonstrate, through analysis of experimental data, the existence of an approximate 'maximum flow frequency' f_c for boundary-layer measurements. Figure 15 shows a comparison of premultiplied energy spectra at $z^+ = 15$ for the
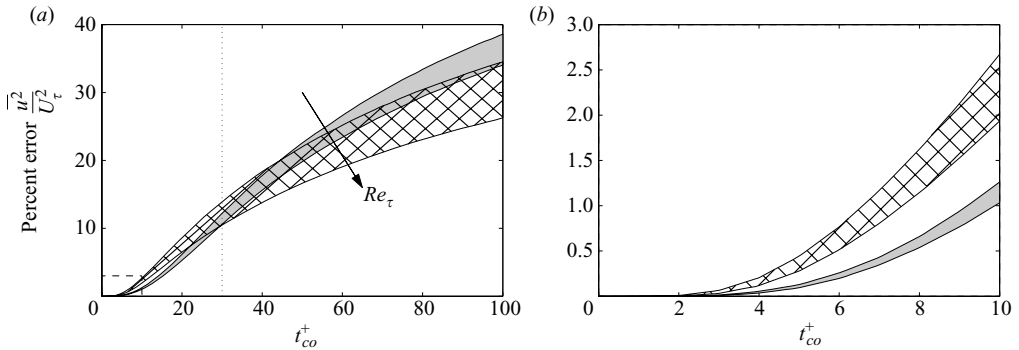
FIGURE 16. Percentage error in $\overline{u^2}/U_\tau^2$ due to a simulated cutoff at t_{co}^+. Data are shown for two wall-normal locations: (shaded region) $z^+ = 15$ and (hatched region) $z^+ = 70$. The filled regions show the spread in percentage error due to the Reynolds number from $Re_\tau = 2820$ (upper bound) to $Re_\tau = 18\,830$ (lower bound). The vertical dotted line shows $t_{co}^+ = 30$. (b) A zoomed detail at small t_{co}^+ (see the dotted line in *a*).

complete set of Reynolds numbers in which non-dimensional wire length is matched ($l^+ = 22$). In terms of the viscous wavelength λ_x^+, figure 15(*a*) indicates that the small-scale end of the spectra collapses well over the range of Reynolds numbers considered (with the only noticeable *Re* effect appearing as ever-increasing amounts of large-scale energy centred around $3 < \lambda_x^+/Re_\tau < 6$). At all Reynolds numbers, the energy is negligible for $\lambda_x^+ \lesssim 30$. In this case λ is defined from a time signal using the local convection velocity U^+. At $z^+ = 15$ the inner-scaled mean velocity profiles fall on to a single curve (with $U^+|_{z^+ = 15} \approx 11$; see the inset in figure 15*a*). Hence, it is easy to understand that these spectra will be similarly well matched in terms of a viscous time scale,

$$t^+ = \frac{tU_\tau^2}{\nu} = \frac{\lambda_x^+}{U^+}, \tag{8.1}$$

as shown in figure 15(*b*). Since the hot-wire data are discrete time series, there is no convection velocity used to calculate t^+ for the abscissa of figure 15(*b*). This plot would imply that (at $z^+ = 15$) turbulent energy is largely contained in scales for which $t^+ \gtrsim 3$. Figure 15(*c*) shows an approximate bounding contour for the full energy map (as a function of z^+ and t^+). The contours show $k_x\phi_{uu}^+ = 0.05$ for all Reynolds numbers with matched $l^+ \approx 22$. (This contour level is shown by the horizontal dotted line in figure 15*b*.) We can see that the high-frequency part of the contours collapses well in terms of t^+ for all Reynolds numbers considered. In addition, it is clear that turbulent information with small t^+ ($\lesssim 10$) is present throughout the log region of the boundary layer, and thus temporal resolution should not be considered as just a near-wall issue. In fact, the smallest time-scale events seem to occur not at the location of the near-wall peak but at $z^+ \approx 70$.

As further proof of an effective maximum flow frequency, figure 16 shows percentage errors in measured broadband intensities due to a sharp spectral cutoff filter applied (during post-processing) at various t^+. Figure 16 is, in effect, constructed by integrating the area beneath the energy spectra such as the ones shown in figure 15(*b*) to the right of a sharp cutoff. The raw fluctuating signals used for this analysis are all temporally well resolved. The frequency response of the anemometer/probe system f_a is in all cases set to approximately 70–100 kHz (as determined by injecting a

2 kHz internal pulse at the bridge), yielding $7.8 > f_a^+ > 1.7$ for $2820 < Re_\tau < 18\,830$. Similarly, the frequency of the analogue low-pass filters f_{lp} is in all cases set to approximately half of the sampling frequency f_s, chosen such that $f_{lp}^+ > 0.94$. Thus, in terms of equipment, there is no obvious temporal constraint on energy that has a time scale larger than $t^+ \approx 1$. Hence, the process shown in figure 16 is analogous to simulating a sharp cutoff due to insufficient anemometer response or poorly chosen low-pass filters. The precise quantitative error is dependent on Re_τ, with the upper bound of the shaded area showing the lowest Reynolds-number result ($Re_\tau = 2820$) and the lower bound showing the highest Reynolds number result ($Re_\tau = 18\,830$). There would also be an expected sensitivity due to l^+ (although in this instance l^+ is constant), since both Re_τ and l^+ will alter the relative proportions of small- and large-scale energy recorded at a given wall-normal location. For figure 16 we show results at only two wall-normal locations: $z^+ = 15$ close to the near-wall peak (shaded) and $z^+ = 70$, which figure 15(c) would indicate is the location of the highest frequency contributions (hatched). Indeed we can see that at smaller t_{co}^+ (figure 16b), the percentage attenuation at $z^+ = 70$ is more acute than at $z^+ = 15$. However, in all instances the form of this curve is the same; namely the error seems to be very small ($<0.1\,\%$), provided that the fluctuations are temporally resolved to $t^+ \approx 3$.

Thus we can establish a maximum flow frequency for boundary-layer measurements of

$$f_c \gtrsim \frac{U_\tau^2}{3\nu}. \tag{8.2}$$

Typical quoted frequency responses of commercially available anemometers are in the range $30 < f_a < 100$ kHz. This imposes an effective Reynolds-number limit beyond which it is unlikely that the smallest scales of u fluctuation (and hence $\overline{u^2}/U_\tau^2|_m$) are correctly resolved. For the most part, the data considered for figures 1 and 2 are within these approximate limits. However, it is noted that the highest Re_τ data of Fernholz *et al.* (1995) will require (by (8.2)) that $f_a > 78$ kHz, which may be close to the limits of some commercial units. By contrast, the data in the HRNBLWT benefit from large viscous scales, and hence comparable Reynolds numbers ($Re_\tau \approx 19\,000$) are fully temporally resolved with a somewhat slower anemometer response of $f_a > 20$ kHz. Regardless, it is clear that some of the laboratory data shown in figures 1 and 2 are approaching an effective Reynolds-number ceiling with conventional anemometer technology. Such considerations become especially pertinent when one considers the results of Khoo *et al.* (1999) and Li (2004), both of which have indicated that the actual response of the combined hot-wire sensor/constant-temperature anemometry system could be up to an order of magnitude less than that indicated by a standard sine/square-wave perturbation test. Also Comte-Bellot (1976) and Freymuth (1977b) have discussed the nonlinear response of hot-wire anemometers, both showing that rapid high-magnitude fluctuations can substantially reduce the useful frequency range of anemometers. In addition to this, the f^2 behaviour highlighted by Saddoughi & Veeravalli (1996) and the transient thermal response of the hot-wire sensor (Morris & Foss 2003) would seem to impose additional limits on the use of anemometers at high frequencies. The solution to this problem probably lies in improved performance anemometry or in 'bigger and slower' facilities; of the latter case, the atmospheric surface layer is an obvious example. (For the study of Metzger & Klewicki 2001 or Kunkel & Marusic 2006 an anemometer response $f_a < 500$ Hz is sufficient to temporally resolve the atmospheric surface layer at $Re_\tau \sim 1 \times 10^6$.)

8.2. *An example of a boundary-layer measurement made with insufficient anemometer response f_a*

The purpose of this section is to highlight the effect on measured turbulence statistics, when an anemometer system imposes a cutoff frequency that is deliberately set to be less than specified by f_c. Note that the wire length is $l^+ = 22$ for all measurements presented here. The only difference is the temporal resolution of the system.

The frequency response of the AN-1003 anemometer was altered by modifying four capacitors (C31, C24, C19 and C5) on the channel board. These alterations were originally made to facilitate balancing the bridge with very small-diameter hot wires (since the ferrite core on the AN-1003 does not provide sufficient adjustment to such small wires). However, it rapidly became apparent that this modification had in fact drastically reduced the frequency response of the anemometer/probe system. For this reason, we eventually used an in-house MUCTA anemometer to make the final measurements with 1.5 μm wires. However, the comparison between the MUCTA and the modified AN-1003 measurements offers useful insight into the detrimental effects of temporal resolution issues. The solid and dashed lines in figure 17(a) show a comparison of the broadband streamwise intensities for the MUCTA and modified AN-1003 channels respectively. Reducing the channel frequency response has resulted in a pronounced attenuation of the intensity profile. Indeed, in spite of the fact that the flow is spatially well resolved ($l^+ \approx 22$), the modified channel exhibits an outer-hump-type behaviour as typified previously by experiments with large l^+. In this case, the additional attenuation is believed to be due to the reduced temporal resolution of the modified bridge. As an example of this, the + symbols show the original temporally well-resolved MUCTA data with a spectral low-pass filter applied during post-processing at a sharp cutoff of $t^+ = 30$. It is noted that other than in the very near wall ($z^+ < 30$) this filtered intensity profile models very closely the actual profile recorded by the modified bridge. Thus a sharp cutoff is proven to be a reasonably effective tool in modelling the effects of temporal resolution on broadband turbulence intensities. Figure 17(b) shows energy spectra at $z^+ = 15$ for the MUCTA, modified AN-1003 and spectrally filtered data. In practice, the modified AN-1003 (dashed curve) does not impose a sharp cutoff at $t^+ = 30$ (as modelled by the spectral filter, shown by the + symbols), producing instead a more gradual attenuation but one that is still loosely centred around $t^+ = 30$. Figure 17(c) shows the missing energy in the modified AN-1003 premultiplied spectra, as compared to the data taken with the MUCTA anemometer. Again, though there is no well-defined sharp cutoff, it is clear that the missing energy is centred around $t^+ = 30$ at all wall-normal locations.

9. Conclusions

New experimental hot-wire data have been presented across a large range of Reynolds numbers ($2820 < Re_\tau < 18\,830$) and with careful matching of the viscous-scaled length of the hot wire. Using these and other previously published data, we have considered the issue of spatial resolution in turbulent boundary layers. The principle findings of this study are summarized by the following points:

(i) *The near-wall peak in inner-scaled streamwise turbulence intensity.* The recorded value of $\overline{u^2}/U_\tau^2|_m$ is subject to the competing effects of the Reynolds number and l^+. As the Reynolds number is increased, there is an increasing presence of large-scale energy in the near-wall region, whilst the small-scale energy remains approximately the same (see §4.1). Thus, the net effect of increasing Re_τ is an increase in the recorded
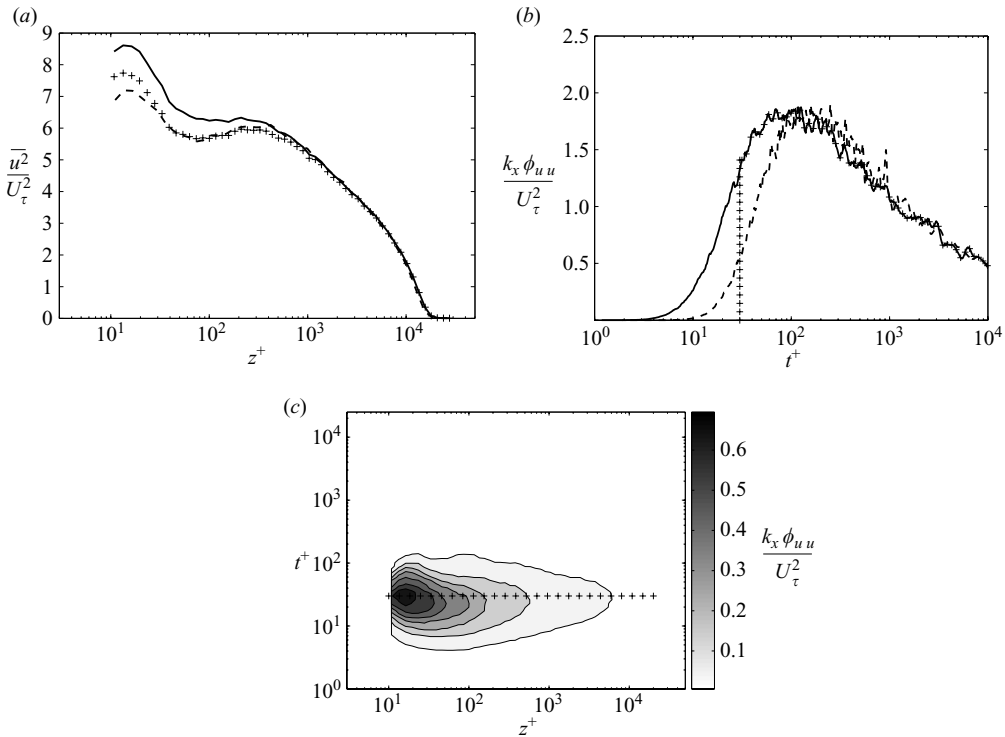
FIGURE 17. (*a*) Broadband turbulence intensity profiles of *u* fluctuation and (*b*) premultiplied energy spectra at $z^+ = 15$ for (solid line) temporally well-resolved data, $l^+ = 22$ and $Re_\tau = 18\,830$, MUCTA anemometer; +, same data spectrally filtered during post-processing at $t^+ = 30$; the dashed line represents modified AN-1003 channel with $l^+ = 22$ and $Re_\tau \approx 18\,000$. (*c*) A map of the missing premultiplied streamwise energy spectra ($k_x \phi_{uu}/U_\tau^2$) for the modified anemometer (as compared to the MUCTA-measured data).

value of $\overline{u^2}/U_\tau^2|_m$. As l^+ is increased, the recorded small-scale fluctuation becomes increasingly attenuated (whilst the recorded large scales are effectively unmodified; see §4.1). Thus the net effect of increasing l^+ is a reduction in the measured near-wall peak $\overline{u^2}/U_\tau^2|_m$. Consideration of these competing effects provides some explanation for the wide scatter exhibited by previous measurements of $\overline{u^2}/U_\tau^2|_m$ (figure 1). When $\overline{u^2}/U_\tau^2|_m$ is plotted against l^+ and Re, the available data seem to lie approximately within a common surface (figure 2). A preliminary empirically derived functional form is provided to describe this surface (3.1).

(ii) *The outer hump in streamwise turbulence intensity*. In this case we show that the so-called outer hump is most likely a symptom of spatial resolution issues, at least for the Reynolds numbers investigated here. No outer peak is present up to $Re_\tau = 18\,830$ for well-resolved turbulent intensity profiles made in the HRNBLWT facility. Only when the length of the wire is increased beyond $l^+ \approx 50$–60 (or when some temporal cutoff is applied; see below) do we begin to see signs of a secondary peak in the broadband intensity profile. Analysis of decomposed statistics (§4.1) and fully mapped energy spectra (§4.2) indicate that the larger wires attenuate the smaller-scale fluctuations and reduce the magnitude of the near-wall peak. The secondary peak in broadband intensity up to $Re_\tau = 18\,830$ is effectively just the large-scale contribution in the

log region, in the absence of the superimposed small-scale activity. It is noted that these attenuated small scales are not solely confined to the near-wall region and extend throughout the log region. Thus the effects of spatial resolution can extend a surprising distance from the wall. At very high Reynolds numbers, the existence of an outer hump should remain an open possibility. If the large-scale energy shown in figure 6 continues to grow indefinitely with Re_τ (whilst the small scale energy remains constant) a genuine outer hump could conceivably emerge in the broadband intensity at some given Re_τ. Note, however, that any such Reynolds number would be very large, since the growth of the log-region energy is slow (approximately scaling as $\log Re_\tau$). Indeed, Marusic, Hutchins & Mathis (2009) and Mathis *et al.* (2009) have recently predicted such behaviour at very high Reynolds numbers, showing through extrapolation of experimental data that the large-scale energy will exceed the near-wall peak at $Re_\tau \approx O(10^6)$. The issue for this study is whether the secondary peak observed in the broadband intensity at lower Reynolds numbers may be due to spatial resolution, and all evidence considered points to such a scenario. However, it is also important to remain open to the possibility that differences may well exist between the broadband intensity profiles of internal and external geometries.

(iii) *The k_x^{-1} region.* As l^+ increases, the region of the premultiplied energy spectrum in which we would expect a self-similar plateau is increasingly eroded by the effects of spatial resolution. Nickels *et al.* (2005) have previously shown that a k_x^{-1} region will only exist close to the wall ($z^+ < 2Re_\tau/105$) and in high-Reynolds-number boundary layers ($Re_\tau > 5250$). Here we add the additional proviso that the k_x^{-1} behaviour will only be evident in the spectra when l^+ is small (~ 20).

(iv) *Kolmogorov-scaled spectra.* Not surprisingly, we find that the Kolmogorov-scaled spectra is also greatly influenced by spatial resolution effects. The appearance of any $-5/3$ behaviour (and subsequent Kolmogorov constant) along with the magnitude of the spectral bump (as noted by Saddoughi & Veeravalli 1994) are all heavily influenced by attenuation due to wire length. In addition, we note that the effects of wire length on the Kolmogorov-scaled spectra extend to considerable distances from the wall and persist to wavenumbers a good deal lower than those which we might assume from simple isotropic assumptions.

(v) *Length-to-diameter ratio (l/d).* At $Re_\tau = 14\,000$ a wire with $l^+ \approx 22$ and $l/d = 100$ experiences a severe attenuation of the near-wall peak ($\overline{u^2}/U_\tau^2|_m$), more in keeping with a much longer wire of length $l^+ \approx 33$ (when $l/d \geqslant 200$). Such results are in keeping with those of LB87. Perhaps more surprising is that insufficient l/d is a considerable source of attenuation throughout the log region, causing a lower broadband intensity (figure 14) and the appearance of secondary-peak-type behaviour at far lower l^+ than for wires with more normal length-to-diameter ratios ($l/d = 200$). This result suggests that for the wire Reynolds numbers considered here, we should exercise caution in any attempts to reduce l/d below the levels recommended by LB87. How these effects extend to higher Reynolds numbers remains an open question.

(vi) *Temporal resolution.* If the experimental system (anemometry and Nyquist filters) cannot resolve time scales down to $t^+ \approx 3$, there will be an additional attenuation of hot-wire-measured energy, over and above that due to spatial resolution and insufficient l/d. When temporal attenuation does occur, it can lead to the pronounced outer-peak behaviour in the broadband streamwise intensities, as was observed previously for wires with large l^+. For most facilities, as the Reynolds number increases, it will become increasingly difficult to guarantee the temporal integrity of

measurements. In unpressurized air, the viscous-scaled time scale $t^+ = 3$ will equate to 100 kHz once U_τ exceeds approximately 2.1 m s^{-1}.

In terms of very simple practical rules, the above conclusions would suggest the following three guidelines for experimentalists:

(*a*) l^+ as small as possible. Careful attention should be paid to this length. Where comparisons are to be made across facilities or Reynolds numbers, it is preferable to do so at matched l^+. Where this is not possible, some attempt should be made to account for the effects of spatial resolution. Provided $l^+ < 20$, the available data suggest that the error in $\overline{u^2}/U_\tau^2|_m$ should be less than 10 % for $Re_\tau \gtrsim 3000$. (This error in turbulence intensity will reduce at higher z^+.)

(*b*) $l/d \geqslant 200$. The errors due to insufficient l/d can be severe. Although it may be possible to relax this value at higher wire Reynolds numbers, until further experimental validation is available, it may be best to err on the side of caution. The present data show that this ratio should definitely not be relaxed to 100 for $Re_w \lesssim 6$.

(*c*) $t^+ < 3$ ($f^+ > 1/3$). The highest frequency information in a turbulent boundary layer will increase as U_τ^2. It is necessary to ensure (as far as is possible) that all experimental apparatus can resolve these time scales. In particular, the anemometer/probe response and the cutoff due to any low-pass filters must exceed this figure.

As a wider point, the use of hot wires with a large degree of spatial attenuation is a useful and insightful experimental technique in its own right. Just as we can learn much from complex signals through the application of filtering techniques during post-processing, the same can also be true when we interrogate turbulent flows using large sensing elements. By selectively skewing our measurements in favour of larger-scale motions, we can uncover subtle phenomena which could otherwise have remained hidden within an overwhelming presence of smaller, more energetic activity. By way of example, the recognition of a Reynolds-number dependence for the near-wall peak in broadband intensity has tended to accompany a parallel recognition of the effects of spatial resolution. Only when we limit ourselves to studying data with small wires ($l^+ \lesssim 10$; Metzger *et al.* 2001; Metzger & Klewicki 2001; Marusic & Kunkel 2003) or attempt to correct for the effects of l (Klewicki & Falco 1990) do such effects become clear. The very fact that some researchers have found no Reynolds-number dependence in $\overline{u^2}/U_\tau^2|_m$, in spite of the fact that the l^+ of their considered data has tended to increase with Re_τ (which one would typically expect to diminish the measured energy), indicates a growing presence of near-wall fluctuations that are relatively impervious to spatial resolution; in other words, there is an increasing presence of large-scale fluctuations in the near-wall region as the Reynolds number increases. Such a presence is an important physical phenomenon and a predicted consequence of certain physical models (i.e. the attached eddy hypothesis of Townsend 1956 and Perry & Marusic 1995; see also the similarity solutions of Marusic & Kunkel 2003). An even more obvious case in which spatially under-resolved flows can provide clues to the underlying physics is in the prominent outer peaks observed when wires with large l^+ are used to measure broadband streamwise intensities. Away from the near-wall region, there is a secondary energetic site, approximately centred in the logarithmic region, in which the energy of very large-scale fluctuations seems to reach a maxima. Traditionally, quite detailed studies of energy spectra are needed to discern these largest scales (e.g. Kim & Adrian 1999; del Álamo *et al.* 2004; Hutchins & Marusic 2007*a,b*). However, by selectively skewing measurements in favour of just the largest scale motions (by under-resolving the small-scale motions), attenuation

due to spatial resolution can uncover a very interesting attribute of high-Reynolds-number shear flows that would otherwise have not been obvious from well-resolved turbulence intensity measurements.

REFERENCES

ABE, H., KAWAMURA, H. & CHOI, H. 2004 Very large-scale structures and their effects on the wall shear-stress fluctuations in a turbulent channel flow up to $Re_\tau = 640$. *J. Fluids Engng* **126**, 835–843.

DEL ÁLAMO, J. C., JIMÉNEZ, J., ZANDONADE, P. & MOSER, R. D. 2004 Scaling of the energy spectra of turbulent channels. *J. Fluid Mech.* **500**, 135–144.

ANDREOPOULOS, J., DURST, F., ZARIC, Z. & JOVANOVIĆ, J. 1984 Influence of Reynolds number on characteristics of turbulent wall boundary layers. *Exp. Fluids* **2**, 7–16.

BAILEY, S. C. C., HULTMARK, M., SMITS, A. J. & SCHULTZ, M. P. 2008 Azimuthal structure of turbulence in high Reynolds number pipe flow. *J. Fluid Mech.* **615**, 121–138.

BALINT, J.-L., WALLACE, J. M. & VUKOSLAVČEVIĆ, P. 1991 The velocity and vorticity vector fields of a turbulent boundary layer. Part 2. Statistical properties. *J. Fluid Mech.* **228**, 53–86.

BARRETT, M. J. & HOLLINGSWORTH, D. K. 2003 Heat transfer in turbulent boundary layers subjected to free-stream turbulence. Part 1. Experimental results. *J. Turbomach.* **125**, 232–241.

BHATIA, J. C., DURST, F. & JOVANOVIĆ, J. 1982 Corrections of hot-wire anemometer measurements near walls. *J. Fluid Mech.* **122**, 411431.

CHAMPAGNE, F. H., SLEICHER, C. A. & WEHRMANN, O. H. 1967 Turbulence measurements with inclined hotwires. Part 1. Heat transfer experiments with inclined hot-wires. *J. Fluid Mech.* **28**, 153–175.

CIMBALA, J. M. & PARK, W. J. 1990 A direct hot-wire calibration technique to account for ambient temperature drift in incompressible flow. *Exp. Fluids* **8** (5), 299300.

COMTE-BELLOT, G. 1976 Hot-wire anemometry. *Annu. Rev. Fluid Mech.* **8**, 209–231.

DEGRAAFF, D. B. & EATON, J. K. 2000 Reynolds number scaling of the flat-plate turbulent boundary layer. *J. Fluid Mech.* **422**, 319–346.

DURST, F., FISCHER, M., JOVANOVIĆ, J. & KIKURA, H. 1998 Methods to set up and investigate low Reynolds nuymber, fully developed turbulent plane channel flows. *J. Fluids Engng* **120**, 496–503.

DURST, F., NOPPENBERGER, S., STILL, M. & VENZKE, H. 1996 Influence of humidity on hot-wire measurements. *Meas. Sci. Technol.* **7**, 1517–1528.

ERM, L. P. & JOUBERT, P. N. 1991 Low-reynolds-number turbulent boundary layers. *J. Fluid Mech.* **230**, 144.

FERNHOLZ, H. H., KRAUSSE, E., NOCKERMANN, M. & SCHOBER, M. 1995 Comparative measurements in the canonical boundary layer at $Re_{\delta_2} \leqslant 6 \times 10^4$ on the wall of the German-Dutch windtunnel. *Phys. Fluids* **7** (6), 1275–1281.

FERNHOLZ, H. H. & WARNACK, D. 1998 The effects of a favourable pressure gradient and of the Reynolds number on an incompressible axisymmetric turbulent boundary layer. Part 1. The turbulent boundary layer. *J. Fluid Mech.* **359**, 329–356.

FREYMUTH, P. 1977*a* Frequency response and electronic testing for constant-temperature hot-wire anemometers. *J. Phys.* E **10** (7), 705–710.

FREYMUTH, P. 1977*b* Further investigation of the nonlinear theory for constant-temperature hot-wire anemometers. *J. Phys.* E **10** (7), 710–713.

GANAPATHISUBRAMANI, B., CLEMENS, N. T. & DOLLING, D. S. 2006 Large-scale motions in a supersonic boundary layer. *J. Fluid Mech.* **556**, 271–282.

Guala, M., Hommema, S. E. & Adrian, R. J. 2006 Large-scale and very-large-scale motions in turbulent pipe flow. *J. Fluid Mech.* **554**, 521–542.

Hancock, P. E. & Bradshaw, P. 1989 Turbulence structure of a boundary layer beneath a turbulent free stream. *J. Fluid Mech.* **205**, 45–76.

Hites, M. H. 1997 Scaling of high-Reynolds number turbulent boundary layers in the National Diagnostic Facility. PhD thesis, Illinois Institute of Technology, Chicago, IL.

Hutchins, N., Ganapathisubramani, B. & Marusic, I. 2004 Dominant spanwise Fourier modes, and the existence of very large scale coherence in turbulent boundary layers. In *Proceedings of the 15th Australasian Fluid Mechanics Conference*, Sydney, Australia.

Hutchins, N. & Marusic, I. 2007a Evidence of very long meandering features in the logarithmic region of turbulent boundary layers. *J. Fluid Mech.* **579**, 1–28.

Hutchins, N. & Marusic, I. 2007b Large-scale influences in near-wall turbulence. *Phil. Trans. R. Soc.* A **365**, 647–664.

Iwamoto, K., Suzuki, Y. & Kasagi, N. 2002 Reynolds number effect on wall turbulence: toward effective feedback control. *Intl J. Heat Fluid Flow* **23**, 678–689.

Johansson, A. V. & Alfredsson, P. H. 1983 Effects of imperfect spatial resolution on measurements of wall-bounded turbulent shear flows. *J. Fluid Mech.* **137**, 409421.

Jørgensen, F. E. 1996 The computer-controlled constant-temperature anemometer: aspects of set-up, probe calibration, data acquisition and data conversion. *Meas. Sci. Technol.* **12**, 1378–1387.

Kasagi, K., Fukagata, K. & Suzuki, Y. 2005 Adaptive control of wall-turbulence for skin friction drag reduction and some consideration for high Reynolds number flows. In *Second International Symposium on Seawater Drag Reduction*, Busan, South Korea.

Khoo, B. C., Chew, Y. T., Teo, C. J. & Lim, C. P. 1999 Dynamic response of a hot-wire anemometer. Part 3. Voltage-perturbation versus velocity testing for near-wall hot-wire/film probes. *Meas. Sci. Technol.* **10**, 152–169.

Kim, K. C. & Adrian, R. 1999 Very large-scale motion in the outer layer. *Phys. Fluids* **11**, 417–422.

Klewicki, J. C. & Falco, R. E. 1990 On accurately measuring statistics associated with small-scale structure in turbulent boundary layers using hot-wire probes. *J. Fluid Mech.* **219**, 119142.

Kunkel, G. J. & Marusic, I. 2006 Study of the near-wall-turbulent region of the high-Reynolds-number boundary layer using an atmospheric flow. *J. Fluid Mech.* **548**, 375–402.

Li, J. D. 2004 Dynamic response of constant temperature hot-wire system in turbulence velocity measurements. *Meas. Sci. Technol.* **15**, 1835–1847.

Li, J. D., McKeon, B. J., Jiang, W., Morrison, J. F. & Smits, A. J. 2004 The response of hot wires in high Reynolds-number turbulent pipe flow. *Meas. Sci. Technol.* **15**, 789–798.

Ligrani, P. M. & Bradshaw, P. 1987 Spatial resolution and measurement of turbulence in the viscous sublayer using subminiature hot-wire probes. *Exp. Fluids* **5**, 407–417.

Löfdahl, L., Stemme, G. & Johansson, B. 1989 A sensor based on silicon technology for turbulence measurements. *J. Phys.* E **22**, 391–393.

Marusic, I., Hutchins, N. & Mathis, R. 2009 High Reynolds number effects in wall-bounded turbulence. In *Proceedings of the the Sixth International Symposium on Turbulence and Shear Flow Phenomena*, Seoul, South Korea.

Marusic, I. & Kunkel, G. J. 2003 Streamwise turbulence intensity formulation for flat-plate boundary layers. *Phys. Fluids* **15**, 2461–2464.

Mathis, R., Hutchins, N. & Marusic, I. 2009 Large-scale amplitude modulation of the small-scale structures in turbulent boundary layers. *J. Fluid Mech.* **628**, 311–337.

McKeon, B. J. & Morrison, J. F. 2007 Asymptotic scaling in turbulent pipe flow. *Phil. Trans. R. Soc.* A **365**, 771–787.

Metzger, M. M. & Klewicki, J. C. 2001 A comparative study of near-wall turbulence in high and low Reynolds number boundary layers. *Phys. Fluids* **13** (3), 692–701.

Metzger, M. M., Klewicki, J. C., Bradshaw, K. L. & Sadr, R. 2001 Scaling the near-wall axial turbulent stress in the zero pressure gradient boundary layer. *Phys. Fluids* **13** (6), 1819–1821.

Mochizuki, S. & Nieuwstadt, F. T. M. 1996 Reynolds-number-dependence of the maximum in the streamwise velocity fluctuations in wall turbulence. *Exp. Fluids* **21**, 218–226.

Monty, J. P. 2005 Developments in smooth wall turbulent duct flow. PhD thesis, University of Melbourne, Victoria, Australia.

Monty, J. P., Stewart, J. A., Williams, R. C. & Chong, M. S. 2007 Large-scale features in turbulent pipe and channel flows. *J. Fluid Mech.* **589**, 147–156.

MORRIS, S. C. & FOSS, J. F. 2003 Transient thermal response of a hot-wire anemometer. *Meas. Sci. Technol.* **14**, 251–259.

MORRISON, J. F., MCKEON, B. J., JIANG, W. & SMITS, A. J. 2004 Scaling of the streamwise velocity component in turbulent pipe flow. *J. Fluid Mech.* **508**, 99–131.

MOSER, R. D., KIM, J. & MANSOUR, N. N. 1999 Direct numerical simulation of turbulent channel flow up to $Re_\tau = 590$. *Phys. Fluids* **11**, 943–945.

NAGIB, H. & CHAUHAN, K. 2008 Variations of von kármán coefficient in canonical flows. *Phys. Fluids* **20**, 101518.

NEKRASOV, Y. P. & SAVOSTENKO, P. I. 1991 Pressure dependence of hot-wire anemometer readings. *Meas. Tech.* **34** (5), 462–465.

NICKELS, T. B. 2004 Inner scaling for wall-bounded flows subject to large pressure gradients. *J. Fluid Mech.* **521**, 217–239.

NICKELS, T. B., MARUSIC, I., HAFEZ, S. & CHONG, M. S. 2005 Evidence of the k_1^{-1} law in a high-Reynolds-number turbulent boundary layer. *Phys. Rev. Letters* **95**, 074501.

NICKELS, T. B., MARUSIC, I., HAFEZ, S., HUTCHINS, N. & CHONG, M. S. 2007 Some predictions of the attached eddy model for a high Reynolds number boundary layer. *Phil. Trans. R. Soc.* A **365**, 807–822.

ONG, L. & WALLACE, J. M. 1998 Joint probability density analysis of the structure and dynamics of the vorticity field of a turbulent boundary layer. *J. Fluid Mech.* **367**, 291–328.

ÖSTERLUND, J. M. 1999 Experimental studies of zero pressure-gradient turbulent boundary-layer flow. PhD thesis, Department of Mechanics, Royal Institute of Technology, Stockholm.

PERRY, A. E. & CHONG, M. S. 1982 On the mechanism of wall turbulence. *J. Fluid Mech.* **119**, 173–217.

PERRY, A. E. & MARUSIC, I. 1995 A wall wake model for the turbulent structure of boundary layers. Part 1. Extension of the attached eddy hypothesis. *J. Fluid Mech.* **298**, 361–388.

PERRY, A. E., MARUSIC, I. & JONES, M. B. 2002 On the streamwise evolution of turbulent boundary layers in arbitrary pressure gradients. *J. Fluid Mech.* **461**, 61–91.

PURTELL, P., KLEBANOFF, P. & BUCKLEY, F. 1981 Turbulent boundary layer at low Reynolds number. *Phys. Fluids* **24**, 802–811.

SADDOUGHI, S. G. & VEERAVALLI, S. V. 1994 Local isotropy in turbulent boundary layers at high Reynolds numbers. *J. Fluid Mech.* **268**, 333–372.

SADDOUGHI, S. G. & VEERAVALLI, S. V. 1996 Hot-wire anemometry behaviour at very high frequencies. *Meas. Sci. Technol.* **7**, 1297–1300.

STEFES, B. & FERNHOLZ, H. H. 2004 Skin friction and turbulence measurements in a boundary layer with zero-pressure-gradient under the influence of high intensity free-stream turbulence. *European J. Mech.* B **23**, 303–318.

TOMKINS, C. D. & ADRIAN, R. J. 2003 Spanwise structure and scale growth in turbulent boundary layers. *J. Fluid Mech.* **490**, 37–74.

TOWNSEND, A. A. 1956 *The Structure of Turbulent Shear Flow*. Cambridge University Press.

UEDA, H. & HINZE, J. O. 1975 Fine-structure turbulence in the wall region of a turbulent boundary layer. *J. Fluid Mech.* **67**, 125–143.

WILLMARTH, W. W. & BOGAR, T. J. 1977 Survey and new measurements of turbulent structure near the wall. *Phys. Fluids Suppl.* **20**, S9.

WILLMARTH, W. W. & SHARMA, L. K. 1984 Study of turbulent structure with hot wires smaller that the viscous length. *J. Fluid Mech.* **142**, 121–149.

WYATT, L. A. 1953 A technique for cleaning hot-wires used in anemometry. *J. Sci. Instrum.* **30**, 13–14.

WYNGAARD, J. C. 1968 Measurement of small-scale turbulence structure with hot-wires. *J. Phys.* E **1**, 1105–1108.